Tectonics®

RESEARCH ARTICLE
10.1029/2025TC009000

From Compression to Extension in the Eastern Pyrenees: New Insights From Low-Temperature Thermochronology

S. Peris[1], **A. Griera**[1], **D. Gómez-Gras**[1], **D. Stockli**[2], **and A. Teixell**[1]

[1]Departament de Geologia, Universitat Autònoma de Barcelona, Bellaterra, Spain, [2]Department of Earth and Planetary Sciences, The University of Texas at Austin, Austin, TX, USA

Key Points:

- The evolution of different tectonic units in the Eastern Pyrenees is addressed by low-temperature thermochronology
- A major cooling event during the Priabonian and Rupelian (35–28 Ma) is still related to orogenic shortening
- The transition period from compression to extension in the Eastern Pyrenees was during the Chattian (28–24 Ma)

Supporting Information:

Supporting Information may be found in the online version of this article.

Correspondence to:

S. Peris,
sabiperis19@gmail.com;
sabi.peris@uab.cat

Citation:

Peris, S., Griera, A., Gómez-Gras, D., Stockli, D., & Teixell, A. (2026). From compression to extension in the Eastern Pyrenees: New insights from low-temperature thermochronology. *Tectonics*, *45*, e2025TC009000. https://doi.org/10.1029/2025TC009000

Received 15 MAY 2025
Accepted 27 DEC 2025

Author Contributions:

Conceptualization: S. Peris, A. Griera, D. Gómez-Gras, A. Teixell
Data curation: S. Peris
Formal analysis: S. Peris
Funding acquisition: A. Griera, A. Teixell
Investigation: S. Peris, A. Griera, D. Gómez-Gras, D. Stockli, A. Teixell
Methodology: S. Peris, D. Gómez-Gras, D. Stockli
Project administration: A. Griera, A. Teixell
Resources: A. Griera, A. Teixell
Supervision: A. Griera, D. Gómez-Gras, A. Teixell

Abstract The tectonic evolution of the Eastern Pyrenees from the orogenic mountain building to the post-orogenic dismantling is still debated. Since the Oligocene, the Gulf of Lion rifting in the Western Mediterranean superimposed crustal extension in this eastern part of the Pyrenean belt, while compressional tectonics persisted in the Central Pyrenees. In this study we use low-T thermochronology to reconstruct the thermal history of the Eastern Pyrenees to provide insights on the distribution and timing of the transition from shortening to extension, which was still poorly resolved. We provide a new data set of (U-Th)/He cooling ages and thermal history models of basement rocks of the Axial Zone of the Pyrenees east of the Tet normal fault. Cooling ages and histories, coupled with an analysis of the lag time between zircon and apatite (U-Th)/He central ages, help in the differentiation of tectonic units (i.e., basement-involved thrust sheets) in the Eastern Pyrenees. Our results support a marked exhumation period during the early Oligocene (35–28 Ma), that we interpret as the last compressional phase. The first extension-related exhumation/cooling occurred during the early Miocene (24–18 Ma) in the footwall of the Tec fault, which was reactivated and propagated south-westwards during the late Miocene (11–5 Ma). Thus, the transition to extension in this region did occur until the late Oligocene, in an interval bracketed between 28 and 24 Ma of relative quiescence or at least slower exhumation rate.

Plain Language Summary The Pyrenees are a mountain belt that originally extended eastwards in what is now the Gulf of Lion (Mediterranean Sea). Due to the opening of the Western Mediterranean, the eastern segment of the Pyrenees was affected by extension and dismantling while in the central and western Pyrenees compression was still ongoing. However, the exact timing of this shift from compression to extension was not well constrained yet. To investigate this, we used thermochronology to analyze the basement rocks of the Eastern Pyrenees. This method tells us the timing when the rocks cooled down as they rose near to the surface, which can then be related with geological processes such as erosion during mountain building, or with extension and normal faulting. Our results show a major cooling event during early Oligocene (ca. 35–28 Ma), and the start of extension mostly during the early Miocene (24–18 Ma), that continued and evolved southwestwards during upper Miocene (11–5 Ma). Therefore, the shift from compression to extension was not immediate, but included a transition period. These findings help us to understand the evolution from formation to dismantling of mountain belts, such as the Pyrenees.

1. Introduction

Understanding the complete evolution of mountain belts requires the study of the processes associated with orogen formation and the causes of their dismantling (e.g., Dewey, 1988; Sun & Murrell, 1994). Although erosion and surface processes play an important role in mountain dismantling and rock exhumation, superimposed extensional tectonics is also an efficient mechanism, as documented in recent examples such as the Ligurian rift (e.g., L. Jolivet et al., 2020), the Aegean Sea (e.g., Lister et al., 1984) or the Basin and Range Province (e.g., Wernicke, 1981). The Alpine Pyrenees provide a good example of the transition from orogenic compressional to subsequent extensional tectonics in a mountain belt, as the easternmost part of the Pyrenees was dismantled and submerged into the western Mediterranean Sea in less than 10 Ma (L. Jolivet et al., 2020). Since the early Oligocene, the Alpine Tethys slab retreat east of Iberia led to the formation of several extensional back-arc basins and the development of the Gulf of Lion (Figure 1), superimposed on the eastern part of the Pyrenean belt (L. Jolivet et al., 2020; L. Jolivet & Faccenna, 2000). Coetaneous with the extensional opening of this western part of the Mediterranean, the shortening was still active in the Central and Western Pyrenees (Labaume et al., 2016), which attests to a diachronic evolution (Figure 1). In between, the Eastern Pyrenees record a superposition of Pyrenean shortening and post-orogenic extensional dismantling, enabling to gain insights into the transition from

Writing – original draft: S. Peris
Writing – review & editing: A. Griera, A. Teixell

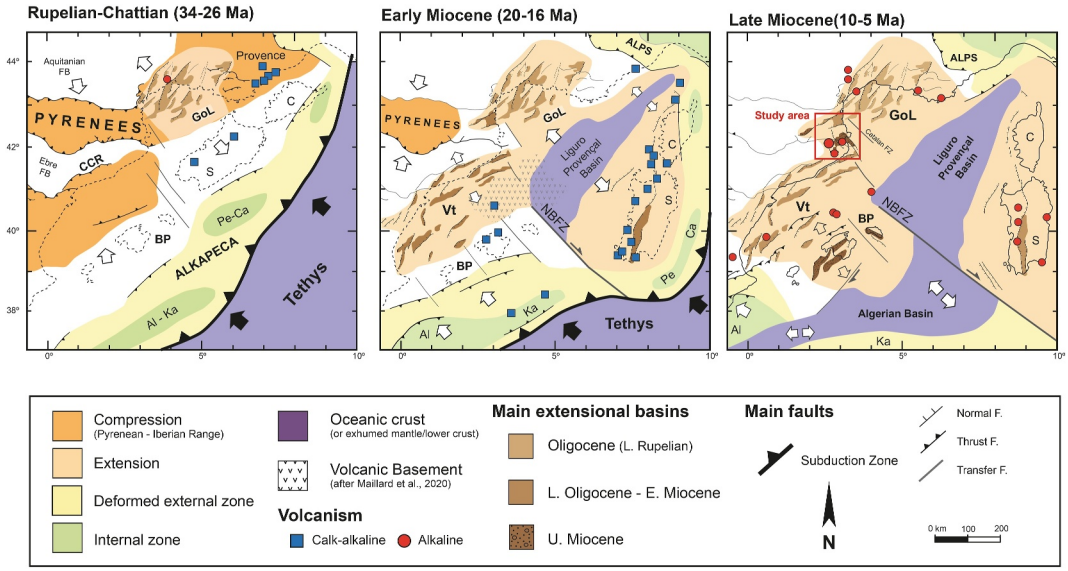

Figure 1. Schematic reconstruction of the Western Mediterranean evolution from the Paleogene to the Neogene in relation with the retreat of the Tethys subducting slab (based on Roca (2001) and Romagny et al. (2020). Volcanism from Martí et al. (1992) and Roca (2001). Abbreviations used: Al: Alboran; BP: Balearic Promontory, C: Corsica, Ca: Calabria; CCR: Catalan Coastal Ranges, FB: Foreland Basin, FZ: transfer fault zone; GoL: Gulf of Lion, Ka: Kabylies; NBFZ: North Balearic Fracture Zone, Pe: Peloritani; S: Sardinia Vt: Valencia Through.

compression to extension. The last episodes of shortening recorded by syntectonic sediments in the South-Eastern Pyrenean basins date from the early Oligocene (younger than 31 Ma) (Carrigan et al., 2016), whereas the timing of transition to the extension is usually poorly constrained and broadly attributed to the late Oligocene and early Miocene (e.g., Angrand & Mouthereau, 2021; Calvet et al., 2021; L. Jolivet et al., 2020; Séranne, 1999; Séranne et al., 2021).

Low-temperature (low-T) thermochronology in the Pyrenees records a rapid cooling event during the early Oligocene (ca. 35–30 Ma), which is recorded along the entire belt from the central (Fitzgerald et al., 1999; Sinclair, 2005) to the eastern part (Gunnell et al., 2009; Milesi et al., 2022). Some authors have proposed that this cooling event was related to late compressional stages (Fitzgerald et al., 1999; Waldner et al., 2021), whereas other authors have proposed that at least in the eastern sector, the cooling was linked to the Gulf of Lion rifting or the West European Rift (Milesi et al., 2022). The significance of the exhumation history in the frame of the transition from compression to extension remains a subject of debate. Thus, the Eastern Pyrenees, which at variance to the Central Pyrenees contains well-characterized extensional structures, becomes a crucial area. In this study, we define the timing and rates of the main Cenozoic cooling events in the Eastern Pyrenees based on apatite and zircon thermochronology, providing new insights on the transition and allowing to discuss the geodynamic implications for the Western Mediterranean evolution.

2. Geological Setting

The Pyrenees were formed by the collision of the Iberian and the Eurasian plates between the late Cretaceous and the early Miocene (Alpine orogeny) (Beaumont et al., 2000; Choukroune, 1989; Ford et al., 2022; Muñoz, 1992; Roure et al., 1989; Teixell, 1998; Vergés et al., 1995, 2002). The Pyrenees can be subdivided into a western, a central and an eastern segment, separated by zones of lateral and oblique thrust ramping. The North Pyrenean Fault (NPF; Figure 2), where existing, is inferred as the suture zone between the Iberian and Eurasian collided margins (i.e., between the Axial and North Pyrenean Zones, Figure 2a).

2.1. Tectonic Framework of the Eastern Pyrenees

Focusing on the Eastern Pyrenees, the North Pyrenean Zone (NPZ) is composed of Mesozoic rocks (locally metamorphosed) and Paleozoic basement massifs (e.g., Agly) that are thrust to the north onto the Aquitaine retro-foreland basin. Toward the south, the Axial Zone is a basement massif made of Paleozoic metasediments

10.1029/2025TC009000

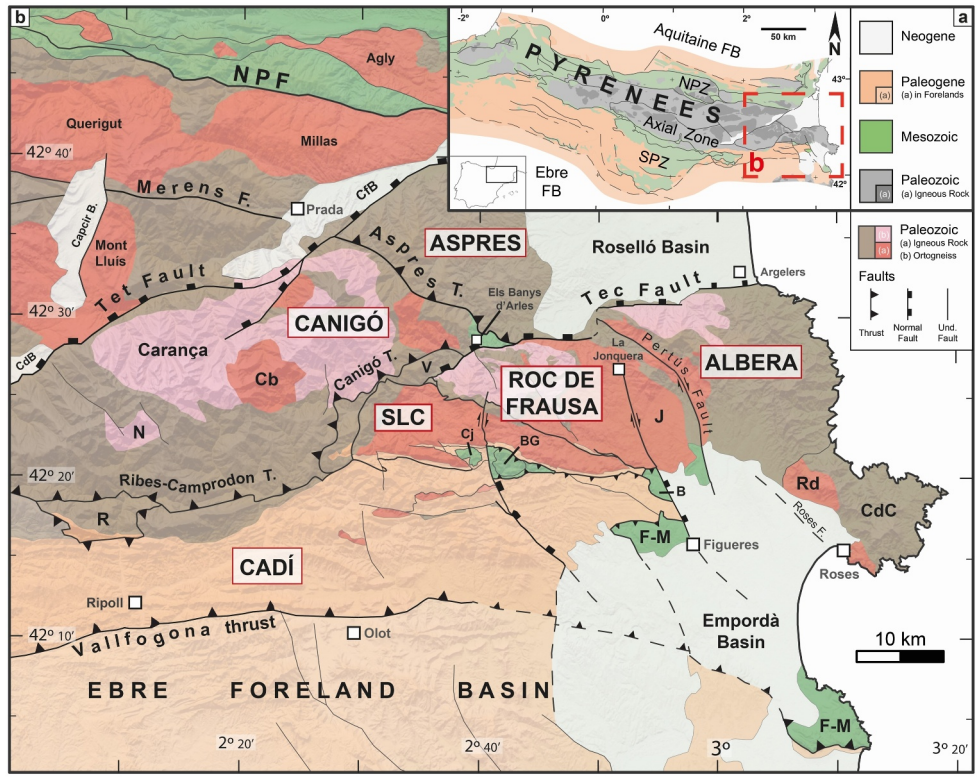

Figure 2. (a) Geologic sketch map of the Pyrenees, with the main tectonic structures and units, and the location of the map in 2B. NPZ: North Pyrenean Zone; SPZ: South Pyrenean Zone; FB: foreland basins. (b) Structural map of the study area in the Eastern Pyrenees, with the name of the tectonic units highlighted (modified from Mapa Geològic de Catalunya, 1:250.000, ICGC, 2021). Abbreviations for Mesozoic units in the SPZ are Cj: Costoja, BG: Bac Grillera, B: Biure, F-M: Figueres-Montgrí. Abbreviations for Paleozoic massifs, Ordovician orthogneisses or Variscan granitoids in the Axial Zone are N: Núria, Cb: Costabona, SLC: Sant Llorenç de Cerdans, V: Vallespir, CdC: Cap de Creus, J: Jonquera, Rd: Rodes. Abbreviations for Cenozoic sedimentary basins are CdB; Cerdanya Basin, CfB: Conflent basin. T: Thrust, F: Fault; NPF: North Pyrenean fault.

(Precambrian-Carboniferous), that are intruded by Ordovician orthogneisses and Late Variscan granitoids. The Alpine architecture of the Axial Zone in the Eastern Pyrenees consists of a crustal-scale thrust stack of south-verging thrust sheets that can be divided into three main units (Figure 2b), which, following Laumonier (2015) and from upper to lower are: (a) the Aspres, (b) the Canigó, and (c) the Albera, Roc de Frausa and Sant Llorenç de Cerdans (SLC) subunits. In this area, the South Pyrenean Zone (SPZ) preserves small klippes of allochthonous Mesozoic rocks over Cenozoic synorogenic sediments forming a thin-skinned thrust-fold-system. The Mesozoic klippes are named from west to east: (a) Costoja, (b) Bac Grillera, (c) Biure, and (d) Figueres-Montgrí (Figure 2b). These relicts are thrust onto in the Ripoll piggy-back basin belonging to the Cadí tectonic unit, which was thrust southwards during the Paleogene (Muñoz et al., 1986). The South Pyrenean Frontal Thrust (SPFT), also named the Vallfogona thrust, represents the leading edge bounding the Ebre pro-foreland basin (Figure 2b). After the orogenic shortening, the Eastern Pyrenees were affected by extensional tectonics (Calvet et al., 2021; L. Jolivet et al., 2020; Milesi et al., 2020, 2023, 2025) that dismantled an ancient, smooth topography (e.g., Birot, 1937; Calvet, 1996), rejuvenating the local relief and creating new Cenozoic basins. The absence of a crustal root and a nearly flat Moho in the Eastern Pyrenees, where there is still a significant mountain elevation, suggest that the region is undercompensated at the crustal level and a thinned mantle lithosphere supports the present-day topography (Chevrot et al., 2018; Gunnell et al., 2008). The regional Tet and Tec NE-SW normal faults formed the Roselló, Conflent, and Cerdanya Neogene basins, dissecting the Axial Zone. In the SPZ, a system of NW-SE normal faults (e.g., Roses fault) created the Empordà basin (Figure 2b).

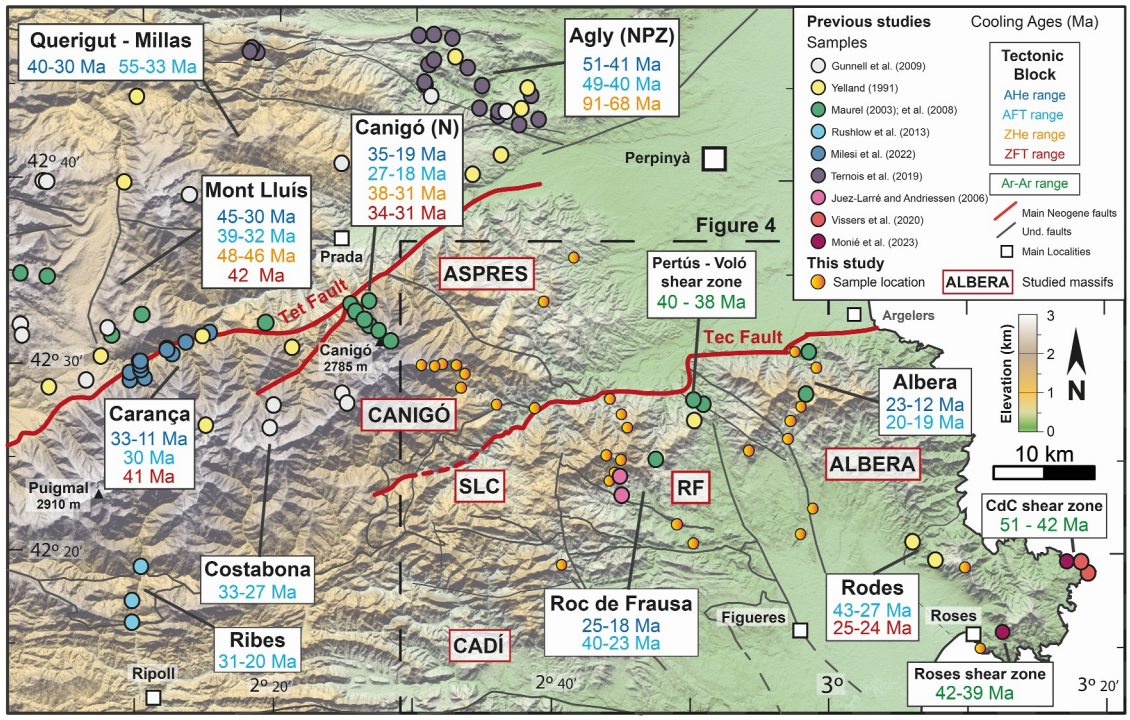

Figure 3. Digital elevation model of the Eastern Pyrenees showing the location of samples and cooling ages obtained in previous studies (Gunnell et al., 2009; Juez-Larré & Andriessen, 2006; Maurel, 2003; Maurel et al., 2008; Milesi et al., 2022; Monié et al., 2024; Rushlow et al., 2013; Ternois et al., 2019; Vissers et al., 2020; Yelland, 1991). See Table S1 in Supporting Information S1 for details and location of samples.

2.2. Previous Data on the Thermal Evolution of the Pyrenees

Prior to the onset of the Pyrenean orogeny, the Iberian and Eurasian margins experienced multiple extensional events in the Triassic-Jurassic and the Early Cretaceous, with the northward propagation of the Atlantic Ocean opening (Vergés et al., 2002 and references therein). The extension led to continental breakup and mantle exhumation (Jammes et al., 2009; Lagabrielle et al., 2010), and was associated with high-temperature gradients that reached 80°C/km during the Cenomanian-Turonian HT-LP peak (Chelalou et al., 2016; Vacherat et al., 2014). Temperatures of 200–400°C may have persisted during the first 30–35 Ma of the subsequent orogenesis due to this inherited thermal perturbation (Angrand et al., 2018; Clerc et al., 2015).

The onset of the Pyrenean convergence has been proposed to be in Late Santonian at ca. ~83 Ma (e.g., Mouthereau et al., 2014; Teixell et al., 2018). The early phase of shortening closed the exhumed mantle domain (Mouthereau et al., 2014; Teixell et al., 2016), bringing both rifted margins into contact and reversing the Aptian-Albian basins at ca. 70 Ma in the Eastern Pyrenean domain (Ford et al., 2016). This event is recorded locally as a first cooling event (70–75 Ma) in the NPZ bedrock (Figure 3) (Agly and Labourd massifs) (Ternois et al., 2019; Vacherat et al., 2014), and also by detrital deposits in the North and South Pyrenean Zones (Beamud et al., 2011; Filleaudeau et al., 2012; Vacherat et al., 2017; Whitchurch et al., 2011). A second orogenic phase is preceded by a tectonic quiescence period (68–56 Ma) during the latest Cretaceous and Paleocene (Calvet et al., 2021; Ford et al., 2016; Grool et al., 2018; Macchiavelli et al., 2017). Then, a main stage of rapid convergence and crustal thickening started at the late Paleocene–early Ypresian (ca. ~56 Ma) recorded by major flexural subsidence in the adjacent foreland basins (Ford et al., 2022). This led to the emergence of the orogen and subsequent subaerial erosion, with a significant sedimentary influx into the Ebre basin, in contrast to the smaller volumes that reached the Aquitaine basin (Fillon et al., 2021; Ford et al., 2022; Ternois et al., 2019). Attending to low-T thermochronology, the related second cooling phase started in the early Eocene (ca. 50–55 Ma) (Bosch et al., 2016; Fitzgerald et al., 1999; Sinclair, 2005), with the maximum cooling peak recorded in the Axial Zone at 35–30 Ma (Figure 3). Several studies support the gradual westward and southward propagation of the orogen emergence (e.g., Calvet et al., 2021; Curry et al., 2021; Ford et al., 2022; Puigdefàbregas et al., 1992; Yelland, 1991).

The maximum cooling peak (ca. 30°C/Ma) during late Eocene–early Oligocene (35–30 Ma) is documented all along the orogen, from the western (Bosch et al., 2016; Guàrdia, 2024; M. Jolivet et al., 2007), to the central (Cochelin et al., 2018; Fitzgerald et al., 1999; Morris et al., 1998; Sinclair, 2005) and eastern Axial Zone (Gunnell et al., 2009; Maurel et al., 2008; Milesi et al., 2022). Most authors interpret this event of rapid cooling (35–30 Ma) as the last pulse of orogenic-driven exhumation. For example, in the Maladeta massif (Central Pyrenees), Waldner et al. (2021) proposed that rapid cooling was originated by the activity of deep basement thrust ramps, since the near massifs located to the north experienced slower cooling rates. On the other hand, Milesi et al. (2022) interpreted this cooling event in the Eastern Pyrenees as attesting the start of extension and normal faulting (at ca. 33 Ma).

Following this generalized exhumation event, cooling rates decreased along a transect of the Central Pyrenees during the Oligocene (30–25 Ma) (Fitzgerald et al., 1999). The last activity of the SPFT at the eastern foreland is inferred from illite fault gouge Ar-Ar dating at 32 ± 4 Ma in the Ter valley (Haines & Van Der Pluijm, 2023), or from the magnetostratigraphic age of the top of the syntectonic Berga conglomerates in Sant Llorenç de Morunys (dated as <31 Ma) (Carrigan et al., 2016). A recent study of U-Pb geochronology on calcite veins propose this is the time of normal faulting in the south-eastern Pyrenees (Cruset et al., 2020), while Parizot et al. (2021) proposed that shortening continued until the early Miocene in the northern Pyrenees in the Corbières area. Thus, the transition from shortening (orogenic) to extension (post-orogenic) in the Pyrenees as deduced from low-T thermochronology and geochronology is still controversial, providing a range spanning between the early Oligocene (~33 Ma) (Milesi et al., 2022) and the early Miocene (~25–20 Ma) (Waldner et al., 2021), and probably varying along strike in the Pyrenean belt.

In the Gulf of Lion, the onset of extension is interpreted to have occurred during the early Oligocene (ca. 32–28 Ma), characterized by the formation of basins with a predominant NE-SW direction (L. Jolivet et al., 2020; Romagny et al., 2020; Séranne, 1999; Séranne et al., 2021), and associated with calc-alkaline volcanism (Martí et al., 1992; Réhault et al., 2012) (Figure 1). Its signature is observed in detrital zircons from the synrift sediments in the SE Provence (Villeneuve et al., 2019). In the Eastern Pyrenees, the Roselló-Conflent basin is inferred to have opened during Aquitanian-Burdigalian (23–20 Ma) (Calvet et al., 2021), linked with the Tec and Tet normal faults (Figures 1 and 2b). Low-T thermochronology from the northern Canigó massif shows an associated cooling event (22–17 Ma; Figure 3) (Maurel et al., 2008; Milesi et al., 2020), even though older ages (27–25 Ma) may indicate it started in the late Oligocene, as suggested by Calvet et al. (2021).

During the late Miocene, a second stage of rifting reactivated older grabens (Roselló basin) and opened new intermontane basins within the Axial zone (Cerdanya and La Seu basins) and the SPZ (Empordà basin). In the Empordà basin, the main faults strike NW-SE contrasting with the general NE-SW trend (Saula et al., 1994) (Figure 1). This NW-SE trend is identical to that of the North Balearic Transfer Zone offshore (Calvet et al., 2021). Low-T thermochronology records a second event of cooling (12–9 Ma) in the western Tet fault (Milesi et al., 2022) and in the eastern Tec fault (Maurel, 2003, p. 200) (Figure 3). A peculiar feature of this second extensional event is the relation with intraplate alkaline volcanism (12 Ma to present) that affected NE Iberia (Empordà, la Selva and Garrotxa areas) (Martí et al., 1992), whose activity is closely linked with the NW-SE normal faults (Bolós et al., 2015; Miranda-Muruzábal et al., 2024; Saula et al., 1994).

3. Methods

Low-T thermochronology is a widely employed technique for quantifying the cooling and exhumation history of rocks in a variety of compressional (Reiners & Brandon, 2006) and extensional settings (Ehlers et al., 2001; Stockli, 2005). Thermochronology aims to time when a specific mineral has cooled below a closure temperature (Tc) and has begun to retain radiogenic daughter products (Reiners & Brandon, 2006; Schildgen et al., 2018). The zone between full retention and full loss of decay products is defined as the Partial Retention Zone (PRZ) (Reiners & Brandon, 2006). Specifically, in this paper we use the (U-Th)/He method for apatite (AHe) and zircon (ZHe) grains. Assuming that the samples were fast-cooled (≥10°C/Myr) (Dodson, 1973), the bulk closure temperature (Tc) for zircon is ~180°C and the PRZ (ZHe PRZ) is between ~200 and 140°C (Guenthner et al., 2013; Hart et al., 2017; Prior et al., 2016; Reiners, 2005; Reiners et al., 2004; Wolfe & Stockli, 2010). For apatite, the bulk Tc is ~60°C and the AHe PRZ is between ~40 and ~75°C (Farley, 2000; Wolf et al., 1996, 1998).

3.1. Sample Strategy and Preparation

Before sampling, a data set on previous low-T thermochronology results from the Pyrenees (Figure 3) was compiled. To improve and complement (U-Th)/He data in the Eastern Pyrenees, we selected locations within distinct tectonic units separated by major faults. We sampled two-sided transects on north and south slopes of the massifs at different elevations following five profiles with a vertical component: (1) Canigó South; (2–3) Albera North and South; and (4–5) Roc de Frausa North and South.

A total of 30 samples (2–3 kg per sample) were collected targeting non-altered igneous rocks, mostly Variscan granitoids or Ordovician orthogneisses and ignimbrites (Figure 3). Heavy mineral separation was done following standard mineral separation procedures. Apatite (AHe) and zircon (U-Th)/He (ZHe) analyses were conducted at the UTChron facility at the University of Texas at Austin (United States), following the procedures described by Prior et al. (2016) for AHe, and Wolfe and Stockli (2010) and Hart et al. (2017) for ZHe (Text S1 in Supporting Information S1). The raw AHe and ZHe ages were corrected for alpha-particle ejection using the Ft correction factor (Farley et al., 1996). A systematic analytical error of 8% for zircon and 6% for apatite was applied to each aliquot based on the replicate analyses of Fish Canyon Tuff zircon and Durango apatite standards (Prior et al., 2016).

3.2. (U-Th)/He Data Set Evaluation and Interpretation

Before proceeding to data interpretation, we evaluated each sample and aliquot to ensure that only reliable analyses are interpreted, following the procedures described by Flowers, Ketcham, et al. (2023), Flowers, Zeitler, et al. (2023). For further detail in the data set evaluation and the plots that were used to identify data patterns and outliers, we refer to Text S2 and Figure S1 in Supporting Information S1. Despite this evaluation, there are still some samples that yielded large intrasample dispersion without any kinetic correlation (e.g., inclusions, size), which could indicate a prolonged period of residence within the PRZ. To accurately represent and statistically characterize individual aliquots from a sample, we assigned to each sample a dispersion value (standard deviation divided by the mean age). The samples with dispersion lower than 20%, which are assumed to be normally distributed, are reported with the mean age and the standard deviation. On the other hand, samples with higher dispersion (>20%) that could represent different intra-sample populations, are evaluated and reported individually as an age range, following Flowers, Ketcham, et al. (2023), Flowers, Zeitler, et al. (2023).

3.3. Inverse Thermal Modeling

Thermal histories were reconstructed using the QTQt software (version 5.8.0; Gallagher, 2012; Gallagher et al., 2009), which uses a Bayesian Markov chain Monte Carlo sampling method to infer sample time-temperature histories (e.g., Milesi et al., 2022; Ternois et al., 2019). Time-temperature (*T-t*) paths fpr different tectonic blocks of the Eastern Pyrenees were only modeled for the profiles, using our new AHe and ZHe data completed with apatite fission track (AFT) data from previous studies (Juez-Larré & Andriessen, 2006; Maurel, 2003). In order to obtain robust results, we followed the strategies explained in Abbey et al. (2023) and Flowers, Ketcham, et al. (2023) for the best decision-making process in planning the model inputs and parameters. For further information, an extended description of the methodology followed is provided in Text S3 in Supporting Information S1.

4. Results

4.1. Apatite and Zircon (U-Th)/He Data

In this section we present the AHe and ZHe ages obtained from 30 samples (Table 1), organized according to their structural position in different tectonic blocks (Figure 4). Single-grain ages and reduced (U-Th)/He data from 115 zircon and 105 apatite grains are reported in Table S2 (Peris, 2025). Thermochronological ages generally increase with elevation, and the slope of the age-elevation profiles are broadly used to estimate apparent exhumation rates. In some cases, a break-in-slope can reveal exhumed PRZ that provide information on the timing of potential changes in exhumation rates (Fitzgerald & Malusà, 2019; Reiners & Brandon, 2006; Stockli, 2005). Nevertheless, the age-elevation approach relies on several assumptions that must be considered if exhumation rates are to be inferred properly (see Reiners & Brandon, 2006). Results are also displayed as age-elevation profiles to estimate

Table 1
Sample Summary Divided by Tectonic Blocks Indicating Location, Lithology, Mean Ages (AHe–ZHe), and Age Range

					AHe		ZHe	
Sample name	Latitude	Longitude	Altitude (m)	Lithology	Age (Ma ± 1σ) (Dispersion %)	Age range (Aliquots)	Age (Ma ± 1σ) (Dispersion %)	Age range (Aliquots)
ASPRES								
SP23-22	42.59842	2.69116	300	Ignimbrite	51.1 ± 9.0 (17.6%)	43.8–63.8 (3)	59.5 ± 13.4 (22.5%)	46.7–79.7 (4)
SP23-24	42.55894	2.65460	630	Ignimbrite	67.7 ± 7.6 (11.2%)	57.1–78.1 (4)	54.1 ± 9.5 (17.7%)	47.3–67.6 (3)
CANIGÓ								
SP21-105	42.46405	2.64406	264	Micaschist	30.1 ± 2.1 (6.9%)	28.0–32.2 (2)	34.8 ± 4.2 (12.1%)	27.8–38.9 (4)
SP21-106	42.46672	2.59817	623	Granite	30.5 ± 3.1 (10%)	27.0–34.4 (4)	32.0 ± 5.4 (16.9%)	25.5–42.4 (6)
SP21-107	42.48176	2.55480	897	Granite	28.3 ± 4.4 (15.7%)	23.9–32.7 (2)	32.2 ± 2.0 (6.1%)	30.3–35.0 (3)
SP21-108	42.49444	2.55956	1101	Granite	26.8 ± 1.0 (3.7%)	25.5–27.8 (3)	26.4 ± 2.5 (9.5%)	23.3–29.0 (4)
SP21-109	42.50206	2.54956	1478	Granodiorite	19.1 ± 1.1 (5.7%)	17.8–20.7 (4)	–	–
SP21-110	42.50296	2.53218	1824	Gneiss	28.8 ± 2.6 (8.9%)	26.2–33.0 (4)	31.9 ± 3.7 (11.5%)	27.6–36.4 (5)
SP21-112	42.50108	2.52299	2096	Augen Gneiss	28.1 ± 2.5 (8.8%)	24.6–30.6 (4)	28.7 ± 2.1 (7.5%)	26.5–31.2 (4)
SP21-113	42.50191	2.50720	2456	Augen Gneiss	29.6 ± 1.7 (5.7%)	27.5–31.7 (4)	30.8 ± 1.0 (3.3%)	29.6–32.1 (3)
ALBERA								
SP22-23	42.37482	2.98020	90	Granite	31.4 ± 3.0 (9.4%)	27.9–35.1 (3)	30.8 ± 2.8 (9%)	26.1–32.9 (4)
SP22-24	42.43693	2.94994	305	Granite	27.6 ± 5.5 (20%)	19.7–34.5 (6)	32.1 ± 4.2 (13%)	29.2–39.3 (4)
SP22-25	42.45304	2.95302	575	Granite	24.4 ± 4.6 (18.9%)	20.7–32.3 (4)	26.9 ± 2.8 (10.5%)	24.4–31.7 (5)
SP22-26	42.46590	2.96615	995	Granite	26.1 ± 1.9 (7.1%)	22.9–27.5 (4)	35.9 ± 2.6 (7.1%)	32.5–39.0 (4)
SP23-39	42.51440	2.95755	145	Augen Gneiss	13.4 ± 3.0 (22.7%)	9.4–17.9 (4)	23.7 ± 1.6 (6.7%)	22.2–25.3 (2)
SP23-40	42.50049	2.98459	620	Augen Gneiss	23.9 ± 5.2 (21.6%)	17.2–31.4 (4)	26.3 ± 1.8 (6.8%)	23.4–28.3 (4)
SP21-70	42.24975	3.18215	4	Granodiorite	27.3 ± 1.7 (6.4%)	25.3–29.4 (4)	31.4 ± 1.7 (5.5%)	28.4–32.8 (4)
SP21-73	42.32197	3.16376	630	Granodiorite	23.3 ± 6.9 (29.7%)	13.5–29.0 (3)	27.1 ± 2.2 (8.3%)	25.0–30.6 (4)
ROC DE FRAUSA								
SP21-78	42.35204	2.96552	106	Granodiorite	32.6 ± 4.1 (12.6%)	27.2–37.1 (3)	42.6 ± 4.0 (9.5%)	37.7–47.7 (4)
SP21-80	42.42632	2.90298	477	Granite	21.4 ± 1.4 (6.3%)	19.4–22.7 (4)	32.5 ± 3.1 (9.6%)	28.9–36.9 (4)
SP21-82	42.39931	2.73489	642	Tonalite	19.1 ± 1.1 (5.9%)	17.8–20.9 (4)	36.6 ± 3.3 (8.9%)	32.7–40.0 (4)
SP21-83	42.40654	2.74070	862	Granodiorite	18.0 ± 2.3 (12.6%)	15.7–21.7 (4)	33.7 ± 2.4 (7%)	31.5–37.6 (4)
SP21-84	42.41781	2.74872	1117	Granodiorite	20.6 ± 1.1 (5.4%)	18.7–21.6 (4)	36.2 ± 5.6 (15.4%)	28.6–43.5 (4)
SP21-85	42.42206	2.73054	1428	Augen Gneiss	–	–	35.0 ± 1.3 (3.8%)	33.7–36.3 (2)
SP21-101	42.47225	2.73497	428	Diorite	6.8 ± 0.4 (6.5%)	6.1–7.2 (4)	26.2 ± 3.1 (11.9%)	22.6–30.7 (4)
SP23-27	42.45861	2.74922	700	Diorite	8.8 ± 1.0 (11.7%)	7.8–10.5 (4)	31.2 ± 2.2 (7.1%)	28.5–33.9 (3)
SP23-28	42.44672	2.75634	1070	Diorite	11.9 ± 1.4 (12%)	10.3–13.8 (3)	34.5 ± 4.0 (11.7%)	28.8–39.2 (4)
SANT LLORENÇ DE CERDANS								
SP21-86	42.34337	2.83603	158	Granite	–	–	62.0 ± 14.4 (23.2%)	40.6–84.5 (7)
SP23-43	42.36057	2.81624	160	Granite	20.1 ± 5.1 (25.3%)	13.8–26.7 (6)	67.8 ± 11.7 (17.3%)	48.5–78.6 (4)
CADÍ								
SP21-88	42.32409	2.67733	653	Granodiorite	17.4 ± 1.4 (8%)	15.6–19.0 (3)	174.6 ± 23.7 (13.6%)	137.9–204.2 (4)

Note. The AHe–ZHe sample data are calculated as mean arithmetic ages with standard deviation (1σ), indicating the intrasample age dispersion in percentage. The age range of single-grain aliquots and the number of grains used for calculation are also shown. The complete single-grain (U-Th)/He reduced data and Ft are reported in Table S2, and openly available in Peris (2025) Mendeley database (https://doi.org/10.17632/7mdyx8xt43.2).

apparent exhumation rates from the slope of the best fitting linear regression for profiles with linear correlation higher than 0.5 (i.e., $r^2 > 0.5$) (Figure 4).

4.1.1. Aspres

North-east of the Canigó massif, two samples were collected from altitudes of 300 and 630 m, respectively. Single grain ZHe ages range from 46.7 ± 2.8 to 79.1 ± 4.8 Ma, while AHe ages range from 43.8 ± 2.6 to 78.1 ± 4.7 Ma (Figure 4), showing large intrasample grain age dispersion (11%–22%; Table 1). Since the elevation difference is relatively small (330 m), the results from the two Aspres samples were interpreted together (SP23-22 and SP23-24).

4.1.2. Canigó

Eight samples of the Canigó massif were collected from the southern slopes between altitudes of 264 and 2456 m (Canigó South, Figure 4). Seven samples provided suitable zircon and apatite grains to analyze, while one sample (SP21-109) furnished only apatites. ZHe mean ages range from 26.4 ± 2.5 to 34.8 ± 4.2 Ma, and AHe mean ages range from 19.1 ± 1.1 to 30.5 ± 3.1 Ma. The Canigó South age-elevation profile does not follow a simple positive exhumation rate; instead, the profile could be divided in two segments (Figure 4). The lower one follows an apparent negative exhumation rate (−0.1 km/Ma), with the older age at the lowest altitude, whereas the upper segment follows a very steep or even negative apparent exhumation rate.

4.1.3. Albera and Cap de Creus

In the Albera subunit, six samples were collected following a two-sided profile in the northern and southern slopes of the massif, ranging from 90 to 995 m of elevation. To the south-east, two more samples were collected from the Cap de Creus subunit (SP21-70 and SP21-73), at 4 and 630 m of elevation (Figure 4). Single-grain ZHe ages obtained range from 22.2 ± 1.3 to 39.3 ± 3.1 Ma, and AHe ages range from 9.4 ± 0.6 to 41.0 ± 2.5 Ma (Table 1). The ZHe and AHe age-elevation profiles from the Albera's southern slope follow a nearly vertical or even negative apparent exhumation rate (Figure 4), with a younger age outlier (SP22-25) in the middle of the profile. On the other hand, the age-elevation trends from the northern slope are more consistent, both AHe and ZHe following a positive apparent exhumation rate of 0.1 km/Ma (Figure 4).

4.1.4. Roc de Frausa

In the Roc de Frausa unit, a two-sided profile from 428 to 1428 m of elevation was sampled, with three samples on each slope and one at the maximum altitude. Single-grain ZHe ages range from 22.6 ± 1.8 to 43.5 ± 3.5 Ma, and AHe ages range from 6.1 ± 0.4 to 21.7 ± 1.3 Ma (Table 1). The northern slope yields an apparent exhumation rate of 0.1 km/Ma for both AHe and ZHe, while in the southern slope the ages of all samples are very similar following an almost nearly vertical slope (Figure 4). East from Roc de Frausa massif, two extra samples were taken between the Jonquera and Pertús faults (Figure 4). The northern sample SP21-80 yields a ZHe age of 32.5 ± 3.1 and AHe age of 21.4 ± 1.4 Ma, similar to the Roc de Frausa samples. Whereas the southern sample (SP21-78) has a ZHe age of 42.6 ± 4.0 Ma and AHe age of 32.6 ± 4.1 Ma, ages that can be considered as transitional with the SLC unit (see below).

4.1.5. Sant Llorenç de Cerdans (SLC) and Cadí

In addition, we collected samples from other tectonic blocks without enough altitude difference to construct age-elevation profiles (Figure 4). These are from the Boadella reservoir area (Sant Llorenç de Cerdans unit, SLC) and a granite exposure within cover sediments of the Cadí unit (South Pyrenean basin) produced by shortcut tectonic inversion. The samples from SLC (SP21-86 and SP23-43) yield ZHe ages ranging from 40.6 ± 3.2 to 84.5 ± 6.8 Ma, and AHe ages from 13.8 ± 0.8 to 26.7 ± 1.6 Ma. The sample of the Cadí unit (SP21-88) yields a AHe age of 20.1 ± 5.1 Ma which is similar to that of the Roc de Frausa unit, and a ZHe age of 174.6 ± 23.7 Ma, being the oldeest cooling age obtained in our study.

4.2. Thermal History Modeling

The thermal evolution of the five profiles was modeled using the QTQt software. The resulting T-t paths were obtained by employing our new AHe and ZHe data, and completed with other thermochronometry data from

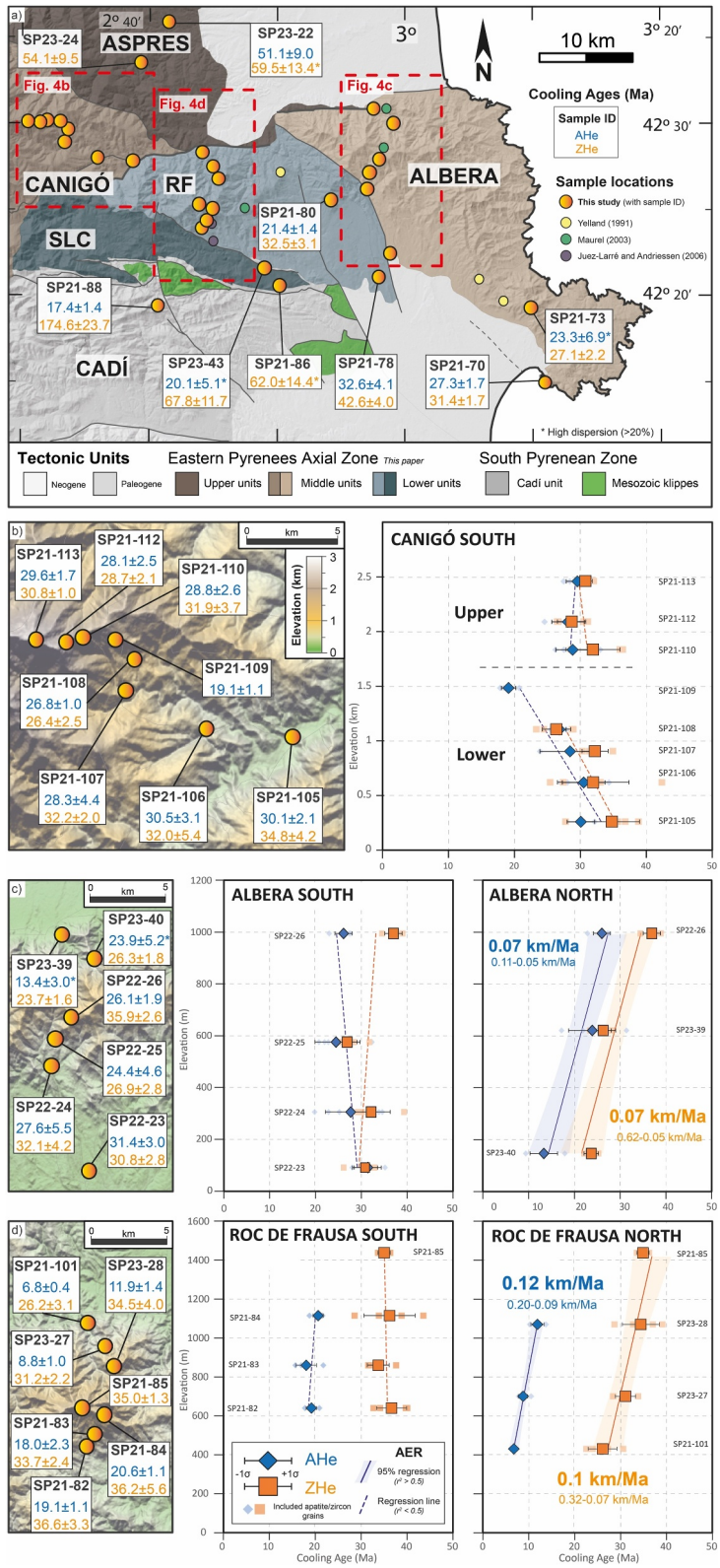

Figure 4. (a) Structural sketch of the alpine tectonic units of the Eastern Pyrenees modified after Laumonier (2015), showing the sample location (from this study and previous studies) with the cooling ages from apatite and zircon (U-Th)/He. Digital Elevation Model showing the cooling ages from (b) Canigó South profile, (c) Albera southern and northern profiles, and (d) Roc de Frausa northern and southern profiles. age-elevation relationship for AHe and ZHe showing the apparent exhumation rates (km/Ma) for each profile. RF: Roc de Frausa, SLC: Sant Llorenç de Cerdans.

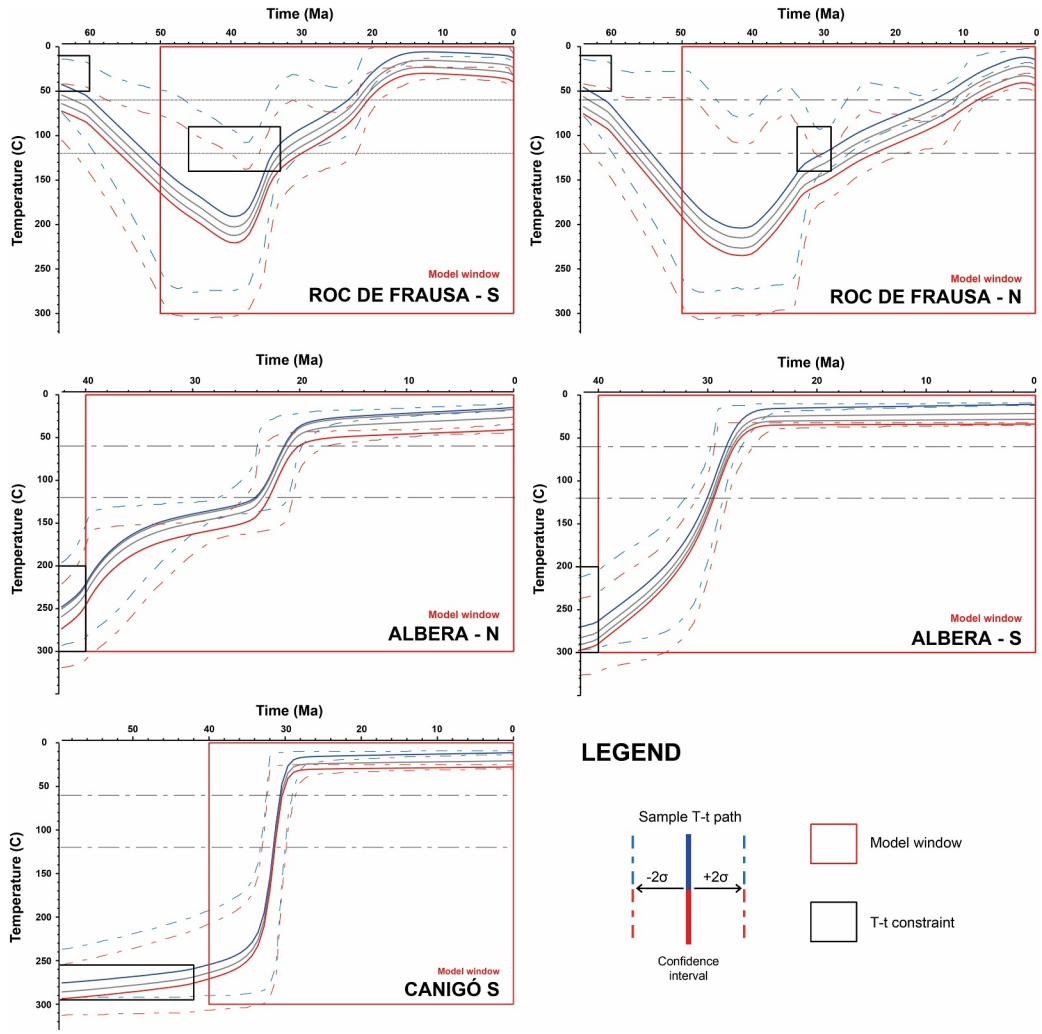

Figure 5. Thermal history models computed with *QTQt* software for the different tectonic units of the Eastern Pyrenean Axial Zone based on our (U-Th)/He profiles with a vertical component. Time-Temperature (*T-t*) paths display the upper (blue) and lower (red) samples, showing the 95% confidence interval (dashed lines). Black boxes represent *T-t* constraints based on Maurel (2003) and Juez-Larré and Andriessen (2006) (see the main text for explanation).

previous studies when available. Further information about the modeling, such as the predicted versus the observed ages, is reported in Figure S2 from the Supporting Information S1.

4.2.1. Canigó South

As indicated above, the Canigó South profile does not follow a positive cooling slope (Figure 4); instead, the lower section of the profile follows a negative slope up to the younger ages observed. Thus, two of the QTQt assumptions are probably not met: (a) all the samples have followed a similar thermal history, and (b) the sample located at the lower altitude has attained the maximum temperature. Therefore, for consistency, only the upper section (SP21-110, -112, -113) of the profile was modeled, comprising samples located at altitudes between 1,824 and 2,456 m.

As an initial T-t constraint we used the modeled cooling history obtained by Maurel (2003) from Ar-Ar in potassium feldspar (FK), with temperature ranges of 275 ± 20°C at 60 ± 18 Ma. In our model (Figure 5), the upper part of the Canigó block experienced an accelerated cooling of ~40°C/Ma between 34 and 29 Ma. Then, since 28 Ma, the upper part of the Canigó block was exhumed without evidence of new burial or/and reheating.

4.2.2. Albera

In the Albera South profiles, the (U-Th)/He ages neither follow a normal (positive) age–elevation gradient (the trend is nearly vertical or even negative for AHe in the lower part) (Figure 4). Furthermore, the intrasample age dispersion is high for both AHe and ZHe (Table 1), which increases the model complexity. Despite this, we performed trial runs with and without the samples/aliquots with higher error, to obtain the best combination for a feasible thermal history including the maximum number of samples. Most of the combinations were giving large errors and we finally used all samples and aliquots (SP22-23, -24, -25, -26).

As an initial T-t constraint we used 250 ± 50°C at 42 ± 2 Ma for the Albera South and North profiles, considering the lower biotite Ar-Ar age range obtained for the Pertús–el Voló shear zone (spanning averaged aged from 39 ± 1.5 Ma to 38.6 ± 0.5 Ma) (Maurel, 2003). The output thermal history of the Albera South profile suggests a constant cooling between 40 and 31 Ma of ∼10°C/Ma, followed by an acceleration between 31 and 28 Ma, with cooling rates near ∼30°C/Ma. Then, the Albera southern slope experienced a period of quiescence with almost no cooling (<1°C/Ma) until the present day (Figure 5). Two samples from Cap de Creus (SP21-70 and 73; Figure 4) also support a fast-cooling event between 31 ± 2 to 27 ± 2 Ma. Thus, the model and two individual samples support an important cooling event during the early Oligocene (∼31–28 Ma).

4.2.3. Roc de Frausa

The initial *T-t* constraint for both the South and North profile models was 30 ± 20°C at 64 ± 4 Ma, since late Cretaceous to Paleocene sedimentary deposits are seen unconformable on the Paleozoic basement, indicating that it was close to the surface at that time. Focusing on the South profile, the age-elevation profile shows a normal steep positive gradient for AHe and ZHe (Figure 4). For the thermal modeling we used all 12 AHe and 14 ZHe ages from four of our samples (SP21-82, -83, -84, -85), and also two AFT ages from Juez-Larré and Andriessen (2006) as *T-t* constraints (115 ± 25°C at 39.5 ± 6.5 Ma). The output thermal model from the Roc de Frausa South profile (Figure 5) shows a continuous reheating up to 230°C at 39 Ma, which is abruptly interrupted by a rapid cooling event between 39 and 34 Ma of ∼20°C/Ma. After a slow cooling (<5°C/Ma) that persisted until 23 Ma, the area was affected by a short second cooling between 23 and 18 Ma of ∼10°C/Ma. A quiescence period of <1°C/Ma then dominates until present. Thus, the southern Roc de Frausa records two main cooling events, the most important between the Priabonian and the Oligocene (39–34 Ma), and the second during the early Miocene (23–18 Ma).

The Roc de Frausa North profile is based on 11 AHe and 13 ZHe data (SP21-85, -101; SP23-27, -28), sharing the upper sample with the southern profile. We used as *T-t* constraint an AFT sample (115 ± 25°C at 31.3 ± 2.4 Ma) from Maurel (2003). After a continuous reheating from the Paleocene up to 240°C at ca. 41 Ma, the output thermal model (Figure 5) records a cooling from 41 to 33 Ma, although the velocity is lower (∼10°C/Ma) than in the southern flank. Then, a constant cooling of ∼4°C/Ma followed until 11 Ma, which was reaccelerated by a slightly faster cooling of ∼7°C/Ma until 5 Ma. Thus, the northern Roc de Frausa also recorded two cooling events, first between the Bartonian and the Oligocene (41–34 Ma), and second during the upper Miocene (11–5 Ma).

5. Discussion

5.1. Interpretation of ZHe and AHe Data and Thermal Models

A first-order observation is that the majority of the obtained ZHe ages indicate a general reset during the Alpine orogeny. Jurassic ZHe ages are only observed in the Cadí unit (SPZ), thereby suggesting it did not experience tectonic or stratigraphic burial to cause zircon reset. In what follows, the thermal history of each tectonic unit is first discussed from north to south and east to west, followed by a discussion of the geodynamic implications.

5.1.1. Aspres Unit

The Aspres unit is an upper basement thrust sheet, allochthonous over the Canigó unit (Laumonier, 2015; Laumonier, Calvet, et al., 2015; Laumonier et al., 2023). Besides, it is part of the footwall of the Tet Neogene extensional fault (Figures 3, 4, and 6). The unit is dominantly constituted by schistose pelitic rocks, and the scarcity of the data set did not allow to carry out thermal modeling. Furthermore, some of the AHe ages are older than ZHe ages obtained from the same sample, implying a large uncertainty due to a presumably complex thermal history (Figure 4 and Table 1). Considering these limitations, ZHe ages in Aspres range between 47 and 80 Ma,

10.1029/2025TC009000

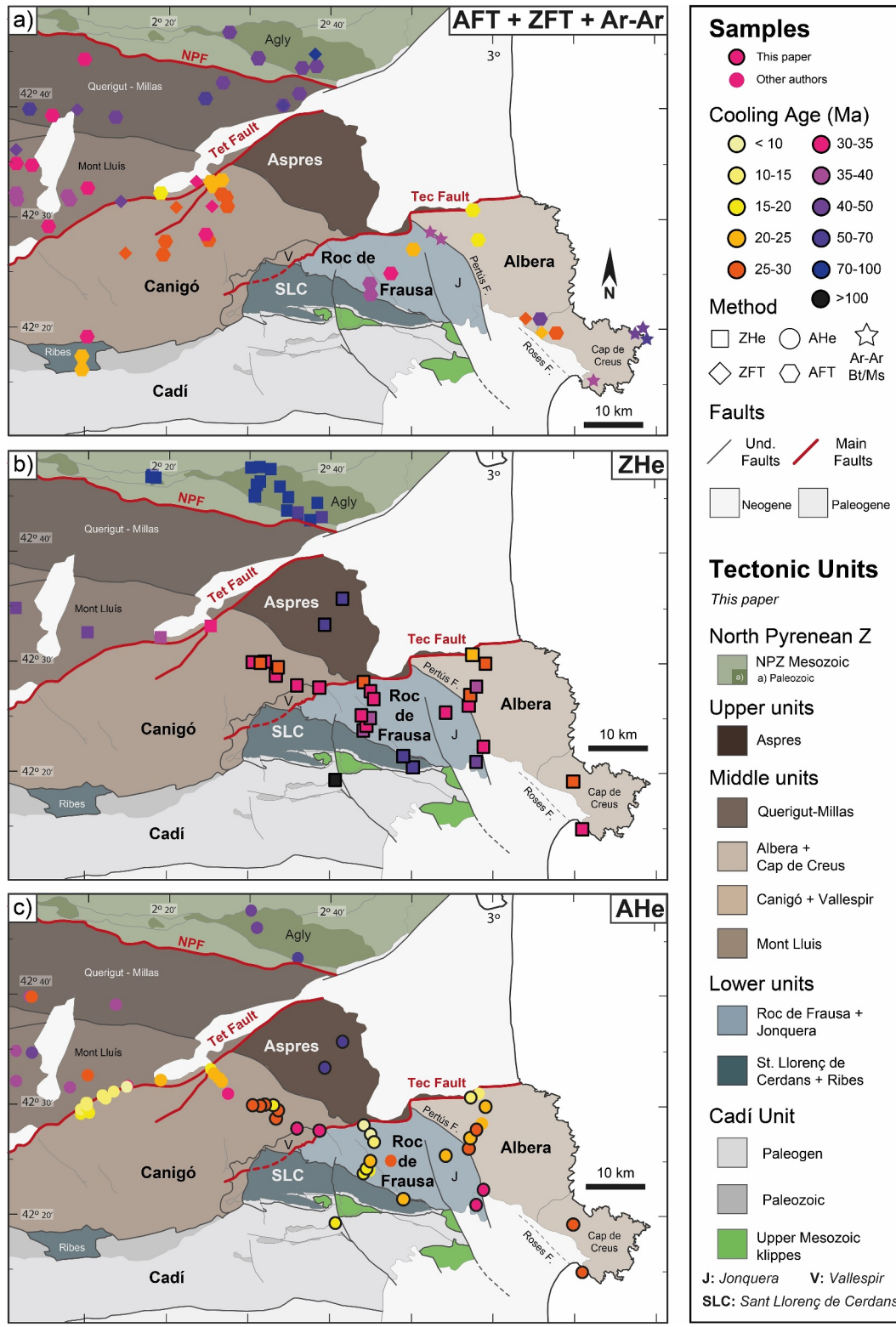

Figure 6. Structural maps indicating the tectonic units of the Eastern Pyrenees, modified from Laumonier (2015), together with the new (U-Th)/He cooling ages from this study and previous thermochronological data: (a) zircon and apatite fission track and muscovite and biotite Ar-Ar, (b) zircon (U-Th)/He, and (c) apatite (U-Th)/He (Gunnell et al., 2009; Juez-Larré & Andriessen, 2006; Maurel, 2003; Maurel et al., 2008; Milesi et al., 2022; Monié et al., 2024; Rushlow et al., 2013; Ternois et al., 2019; Vissers et al., 2020; Yelland, 1991). See Table S1 in Supporting Information S1 for details and location of samples.

10.1029/2025TC009000

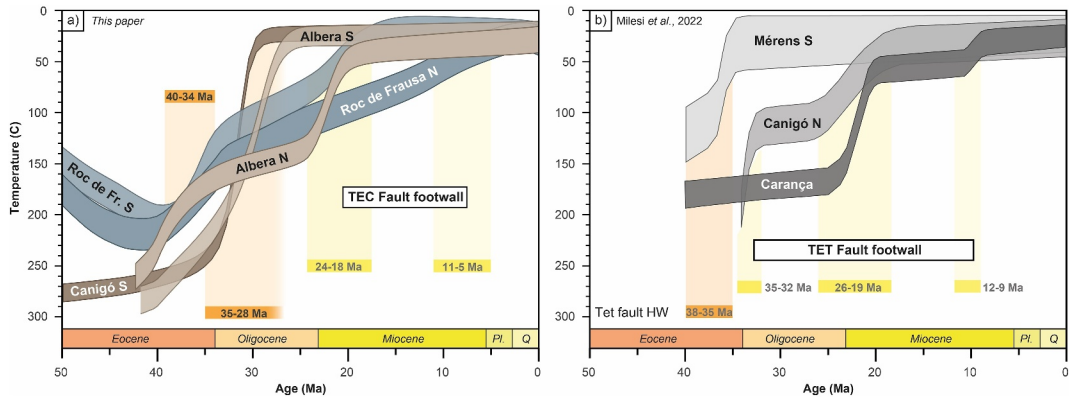

Figure 7. Thermal modeling summary. (a) Compilation of the output thermal histories for the study area: Albera North and South, Roc de Frausa North and South, and Canigó South. (b) Compilation of the output thermal histories and the main cooling events from Milesi et al. (2022) in the Tet fault hanging wall: Canigó North, Carança and Mérens South (Mont-Lluís). In all cases, thermal models were computed using *QTQt* software. Main cooling events are represented as vertical bands, highlighting the interpretation of the tectonic regime: compression (orange) or extension (yellow).

while the AHe mean ages between 44 and 64 Ma (Figure 6). These ages are the oldest obtained from the eastern Axial Zone, and older than those from a similar altitude in the Canigó block. Both AHe and ZHe ages record a large age dispersion, but two main populations are identified: an older one between 63 and 80 Ma (Late Cretaceous) and a younger one ca. 45 Ma (Mid Eocene) (Table SP1). The younger age population (ca. 45 Ma) is similar to that observed in the North Pyrenean unit of Agly (Figure 6) (Ternois et al., 2019), where AHe and AFT ages range from 40 to 51 Ma (Gunnell et al., 2009). Late Cretaceous cooling is not reported for any of the other basement units of the Eastern Axial Zone.

The coexistence of various populations of AHe and ZHe from the Late Cretaceous to the Mid Eocene may be related to multiple factors. The older ages could represent the cooling due to the onset of contraction and plate convergence. Nevertheless, caution is required when interpreting these results in the geodynamic context of the Pyrenees. An alternative possibility is that the large age dispersion has been caused by the Aspres unit residing for a certain time within the zircon and/or apatite PRZ. Given the limitations of the current data set, it is not possible to provide quantitative constraints.

Despite the uncertainty, the results obtained are consistent with the interpretation put forth by Laumonier (2015) and Calvet et al. (2021) that the Aspres thrust sheet corresponds to an uppermost thrust unit emplaced during the initial stages of Alpine convergence, which implies that the Aspres and Merens faults are distinct tectonic structures (Figures 3 and 6), in contrast to the tectonic map proposed by ICGC (2024).

5.1.2. Canigó Unit

The Canigó thrust sheet is the largest of the eastern Axial Zone, and according to Calvet et al. (2021) was emplaced during mid Lutetian to Bartonian times. The unit is bound to the west of the Neogene Tet fault, separating it from the Mont Lluis massif in the fault hanging wall (HW) (Figure 6). The nearest footwall of the Tet fault on the northern slopes of the Canigó massif has been intensively studied in recent years with low-T thermochronology (Maurel, 2003; Maurel et al., 2008; Milesi et al., 2020, 2022, 2023) (Figures 3 and 6). From these studies (Figure 7), a first cooling is inferred during the Priabonian-Rupelian interval in the northern Canigó, the onset of which is not well-constrained but it ended ca. 30–33 Ma. A second cooling was recorded between the late Oligocene and early Miocene (26–19 Ma) and was interpreted to be related to the Neogene activity of the Tet fault.

Our Canigó South profile, located on the southern slopes of the massif, provides new thermochronological constraints for the unit. The obtained ZHe mean ages range from 35 to 26 Ma, while the AHe mean ages are between 31 and 27 Ma (Table 1). We have found that the age-elevation profile does not follow a normal positive exhumation rate (Figure 4). Instead, the profile could be divided into two segments, and the sample separating both (SP21-109) is located close to mapped faults (Laumonier, 2015, after Guitard et al., 1992; Laumonier, Le

Bayon et al., 2015; Wiazemsky et al., 2010), and is characterized by the youngest AHe cooling age (ca. 19 Ma). A localized heat transfer due to fluid flow advection through extensional fractures could explain this anomaly, in a similar way than was deduced by Milesi et al. (2020) in the vicinity of the Tet fault. However, vertical or negative exhumation trends are also observed in the southern slopes of the Albera and the Roc of Frausa profiles (Figure 4), and a more general explanation appears necessary.

The rapid cooling between 34 and 29 Ma (~40°C/Ma) recognized in several of our models is consistent with the cooling age obtained by Milesi et al. (2022) in the northern Canigó block (ca. 35–32 Ma). AHe and ZHe ages obtained in the lower segment of the Canigó South profile are within the same range (Figures 4 and 5), indicating that this region crossed the apatite and zircon PRZ around the same time (ca. 30 Ma). However, uncertainty in the thermal history interpretation is large because the area may have been affected by late faults and/or block rotation during extension. Despite this, our Canigó South profile records a single cooling event, while a second cooling stage during the late Oligocene and early Neogene, such as observed in the northern Canigó area near the Tet fault (26–19 Ma; Figure 7) by Milesi et al. (2020, 2022) and Gunnell et al. (2009), is not detected, although it cannot be discarded.

5.1.3. Albera Unit

The Albera massif is the easternmost thrust sheet of the Eastern Pyrenees (Figure 6), bounded in the north by the Tec normal fault, the Empordà basin in the south, and in the west by the Pertús shear zone (Figure 2b). The range of values obtained in the northern flank of the massif are 24–36 Ma for ZHe and 13–26 Ma for AHe. The AHe values are similar to those obtained by Maurel (2003). Both the ZHe and AHe profiles display parallel positive trends, with exhumation rates around 0.07 km/Ma. Furthermore, all ages become younger toward the Tec fault (Figure 5), a trend characteristic of footwall blocks of active normal faults (Stockli, 2005).

In the Albera South profile, AHe mean ages range from 31 to 24 Ma, while ZHe ages range from 36 to 27 Ma (Figure 4). This similarity between both ZHe and AHe ages suggests a rapid cooling event, which is supported by the ZHe profile that follows a nearly vertical or positive exhumation path (Figure 4). Furthermore, the similar values of our AHe and ZHe and the younger suites of ZFT and AFT (27–24 Ma) recorded by Juez-Larré and Andriessen (2006), point to comparable ages from all low-temperature thermochronometers, which suggests the occurrence of a rapid cooling event in this area during the Oligocene. However, the AHe profile yields an apparent negative exhumation trend, with the older age in the lower altitude (SP22-23) and the youngest age in the middle (SP22-24), both near Neogene faults. Therefore, the significant AHe intrasample dispersion may be indicative of partial resetting during different cooling periods, accounting for a complex thermal history resulting from the Alpine thrusting event and the reworking by the Neogene extensional faulting.

The results from thermal modeling reaffirm these interpretations. For the southern flank of the Albera massif, a slow and constant cooling from 40 to 30 Ma is inferred, followed by an acceleration between 30 and 27 Ma (Figure 5). On the other hand, the thermal model from the northern flank, where AFT constraints from Maurel (2003) were used, records a first cooling from 40 to 35 Ma, and a second fast cooling event from 24 to 20 Ma, both separated by a rather slow cooling period (<3°C/Ma; Figure 5). Both age-elevation profiles and thermal models point to at least two cooling pulses. A first Eocene-Oligocene event, with a similar age to that observed in the Canigó unit, is better recorded in the Albera South profile than the Albera northern flank, while a second cooling event is only recorded during the early Miocene phase (24–20 Ma) in the northern flank. Consistently with syntectonic Ar-Ar biotite ages obtained by Maurel (2003) in the Pertús transpressive shear zone (ca. 39–38 Ma), we infer that the first cooling event is related to the Alpine compression. The second event can be attributed to rotation in the footwall of the Tec normal fault (Figure 7), with an age similar to those published in the footwalls of the Tet and Py faults by Milesi et al. (2020, 2022). This interpretation is also consistent with syntectonic sedimentation during the early Miocene in the adjacent Conflent and Roselló basins (Calvet et al., 2021), and furthermore, supports that the eastern sector of the Tec fault was active at least until the late Miocene (13 Ma).

Finally, the thermal history deduced for the Albera unit does not favor a correlation between the Pertús fault and the Aspres basal thrust (as proposed in the tectonic map by ICGC, 2024), since the Aspres unit has much older cooling ages. Due to the similarity between the AHe and ZHe cooling ages from the Albera South and the Canigó South profiles, we propose these two units share a similar thermal history during the Paleogene exhumation, which could indicate that form part of the same Alpine thrust sheet (Canigó-Albera). Additionally, this would

suggest that the Paleozoic basement of the upper Alpine thrust sheets (e.g., Aspres) have no continuity in regions currently located south of the Tec fault, the upper sheets being preserved only in the frontal Mesozoic klippes of the SPZ.

5.1.4. Roc de Frausa Unit

The Roc de Frausa unit is bounded to the north by the Tec fault and is in thrust contact toward the south with the SLC unit and the SPZ (Cadí unit; Figure 6). Both ZHe and AHe age-elevation profiles follow a positive (north) or vertical (south) exhumation rate (Figure 4), while ages young toward the Tec fault, evidencing its activity. The western sector of the Tec fault at Roc de Frausa was active at least until the late Miocene (6 Ma), in contrast with the eastern sector (Albera massif), where the youngest age observed is 13 Ma (Figure 4). This suggests a westward propagation of the Tec fault activity, similar to that of the Tet fault, which propagated south-westwards from the Conflent to the Cerdanya basins during the Neogene (e.g., Milesi et al., 2020).

Despite the similar ZHe cooling ages in the Roc de Frausa with the observed the Albera and Canigó units (37–26 Ma in the Roc de Frausa case), the southern flank of Roc de Frausa yields much younger AHe ages (ca. 20 Ma). The age gap between the two thermochronometers may be attributed to a single, slow cooling phase, or alternatively it could reflect a quiescence period between two cooling events. The comparable AHe age (ca. 20 Ma) of southern Roc de Frausa, SLC and Cadí units provides evidence for a significant cooling event during the early Miocene affecting both the Axial and South Pyrenean Zones (Figure 6c). Considering the early Oligocene cooling event observed in the nearby Albera and Canigó units, it can be inferred that at least two main cooling events have occurred. If this interpretation is correct, the Roc de Frausa is the only unit for which an upper Paleogene quiescence period has been identified, a period that was also deduced for the northern flank of the Canigó massif by Milesi et al. (2022) (Figure 7).

The thermal modeling also supports the hypothesis of two cooling events (Figure 7). First, a fast cooling recorded by ZHe (40–34 Ma), followed by a quiescent or slow cooling period, and then a second abrupt cooling between 20 and 18 Ma recorded by AHe. Each cooling event is represented by each method (ZHe and AHe), which means that during the quiescence (or slow cooling) period (34–20 Ma) the region was at least below the apatite PRZ. In contrast, the northern Roc de Frausa model (Figure 7) shows a constant slow cooling from the Oligocene to the mid Miocene, with a slight re-acceleration until the Pliocene (~7°C/Ma).

5.1.5. Sant Llorenç de Cerdans (SLC) and Cadí Units

At SLC AHe ages range from 27 to 14 Ma, while the ZHe ages are between 85 and 41 Ma. Even though the Roc de Frausa profile is only a few kilometers north, the recorded ZHe cooling ages are clearly older, and for this reason, we differentiate this unit from the Roc de Frausa unit, supporting the structural interpretation by Laumonier (2015) (Figure 6). However, the boundaries of both units have been slightly adjusted, extending the SLC unit eastwards until the locality of Biure (Figure 6). Besides, high intrasample age dispersion (>20%) and a gentle negative ZHe age-eU correlation is observed in the two samples of this unit (Table 1, SP1 and SP2), which could represent a slow cooling, longer residence time, or reheating and partial resetting in the PRZ (e.g., Flowers, Zeitler, et al., 2023). In contrast, the AHe mean cooling age is similar to those observed in the southern Roc de Frausa profile (ca. 20 Ma). Thus, after the Paleocene cooling age recorded (ca. 60 Ma), we interpret that the SLC unit experienced limited burial with only partial resetting. This can indicate that the leading edge of the overlying basement nappe stack did not reach the sampled part of the SLC unit during the orogeny, in contrast with the Roc de Frausa, Canigó and Albera units which do show reset ZHe ages that we attribute to thrust stacking. After that, the region experienced a similar Neogene thermal history with a marked early Miocene cooling event (ca. 20 Ma).

The sample from the Cadí unit records an AHe mean age of 17 Ma, similar to but slightly younger than the Roc de Frausa. In contrast, the ZHe mean age of 175 Ma, is the oldest Mesozoic cooling age that we obtained. This cooling age indicates that the Paleozoic basement in this area was not reset during the Pyrenean orogeny, and the Cenozoic sedimentary cover was not thick enough to reach the zircon PRZ. However, it crossed the apatite PRZ, and the AHe datum indicates that the region experienced a similar Neogene thermal history than the Roc de Frausa and SLC units.

5.2. Difference Between ZHe–AHe Ages Δ(ZHe-AHe) and the Role of Normal Faults

To interpret the spatial distribution of thermochronologic data across tectonic units and the role of normal faulting in the northern and southern slopes of the basement massifs, two topographic profiles with (U-Th)/He data were constructed through the Roc de Frausa-Canigó massifs and the Albera massif (Figures 8b and 8c). These profiles allow to elucidate the influence of the Neogene faults of Tec and Tet during cooling and their potential role for heat advection. Additionally, we considered the difference between the ZHe and the AHe age for the same sample (Figure 8a), the ZHe–AHe age lag Δ(ZHe-AHe), which gives an approximation of the behavior of the different tectonic blocks in between they crossed the ZPRZ and the APRZ. The Δ(ZHe-AHe) is used as a first-order estimate of the thermal history and is a proxy for the main event of exhumation and the cooling velocity for each tectonic unit.

Comparing the spatial distributions of Δ(ZHe-AHe), it is possible to detect a significant variation across the different tectonic blocks (Figure 8a). The Δ(ZHe-AHe) is small in most samples of the southern Canigó and Albera units (∼0 to 5 Ma), which supports the interpretation that both units share a similar Paleogene thermal history, with a fast Priabonian-Rupelian cooling (35-28 Ma) crossing both apatite and zircon PRZ. On the other hand, the Δ(ZHe-AHe) in Roc de Frausa is higher in all samples (>10 Ma), especially in the northern slope (∼22 Ma). Therefore, the Roc de Frausa remained below the apatite PRZ at least until the early Miocene cooling (ca. 20 Ma). Finally, the highest lags are found in the samples from the SLC and Cadí units, which have a Δ(ZHe-AHe) of 48 and 160 Ma respectively, and indicate the partial or null resetting of ZHe observed in the SPZ during Alpine orogeny. These contrasting Δ(ZHe-AHe) patterns observed in the Eastern Pyrenees (Figure 8a) reflect distinct exhumation histories. On one hand, in the Canigó and Albera units, the near overlap of AHe and ZHe ages suggests relatively rapid exhumation through both the zircon and apatite PRZs during the early Oligocene. We interpret this as being driven by shortening-associated with the Pyrenean orogeny. On the other hand, the Roc de Frausa massif exhibits a consistent ∼10 Ma offset between Zhe and AHe ages, which we interpret as evidence for a prolonged residence below the apatite PRZ following the Pyrenean orogeny. This suggests a subsequent phase of tectonic quiescence or slower exhumation. A similar, though less pronounced, pattern is observed in the Albera massif, where the AHe–ZHe age offset is smaller (∼5 Ma) and increases from south to north, particularly in samples located near the Tec fault. This spatial variation in Δ(ZHe-AHe) is further consistent with the westward propagation of the Tec fault, as suggested by thermal modeling (Figure 7), and may reflect localized heat advection and cooling in the footwall block.

The Tec and Tet faults are the larger Neogene normal faults in the Eastern Pyrenees. The throw of the Tet fault was estimated approximately in 2–3 km in the Conflent basin, and that of the Tec fault is ca. 1,600 m in the Roselló basin, with a displacement that decreases south-westwards (Calvet et al., 2021; Lacan & Ortuño, 2012). According to Laumonier (2015), the strike variation of the Tec fault from E-W direction to NE-SW (Figure 8a) is interpreted as inherited from the Alpine thrust configuration. From the topographic profiles in Figures 8b and 8c it is possible to infer the range of influence of Neogene normal faults in the local cooling/exhumation. In the Roc de Frausa-Canigó profile (Figure 8b), the Tec fault produces an abrupt jump of ZHe and AHe ages from older in the HW to younger in the footwall. Besides, the cooling ages in the footwall young toward the fault (approx. 10–15 Ma younger cooling ages), a feature also observed in the northern flank of the Albera and reported in the Canigó units by Milesi et al. (2020) (Figures 8b and 8c). This observation could represent a fault-related influence (which spans for approximately 5 km) of heat advection and posterior cooling in the footwall (Stockli, 2005) (Figures 8b and 8c). However, it is worth noting that the apparent exhumation rates calculated from low-T thermochronometers may not be purely due to rigid-body, homogeneous tectonic uplift, but may also result from other factors, such as footwall tilting and rotation (Johnstone & Colgan, 2018; Stockli, 2005). Since footwall rotation is likely during the Neogene extension, its potential impact on the thermochronologic ages and thermal models is addressed with greater detail in Section 5.3.

The apparent exhumation rate of ∼0,1 km/Ma obtained for the northern flanks of the Albera and Roc de Frausa are consistent with the ones calculated in the Tet fault footwall of ∼0,1–0.3 km/Ma by Milesi et al. (2022). To take these values as meaningful we must assume that the isotherms remained near-horizontal or in a dynamic advective equilibrium controlled by tectonic exhumation (Stockli, 2005). The thermal field can be locally perturbed by plutonism or hydrothermalism, and evidence for geothermal activity has been recently reported for the Tet fault footwall by Milesi et al. (2020). These authors observed that AHe ages can be impacted by local hydrothermal perturbation, although this is restricted to the vicinity of hot springs. Since our samples were collected far from the

10.1029/2025TC009000

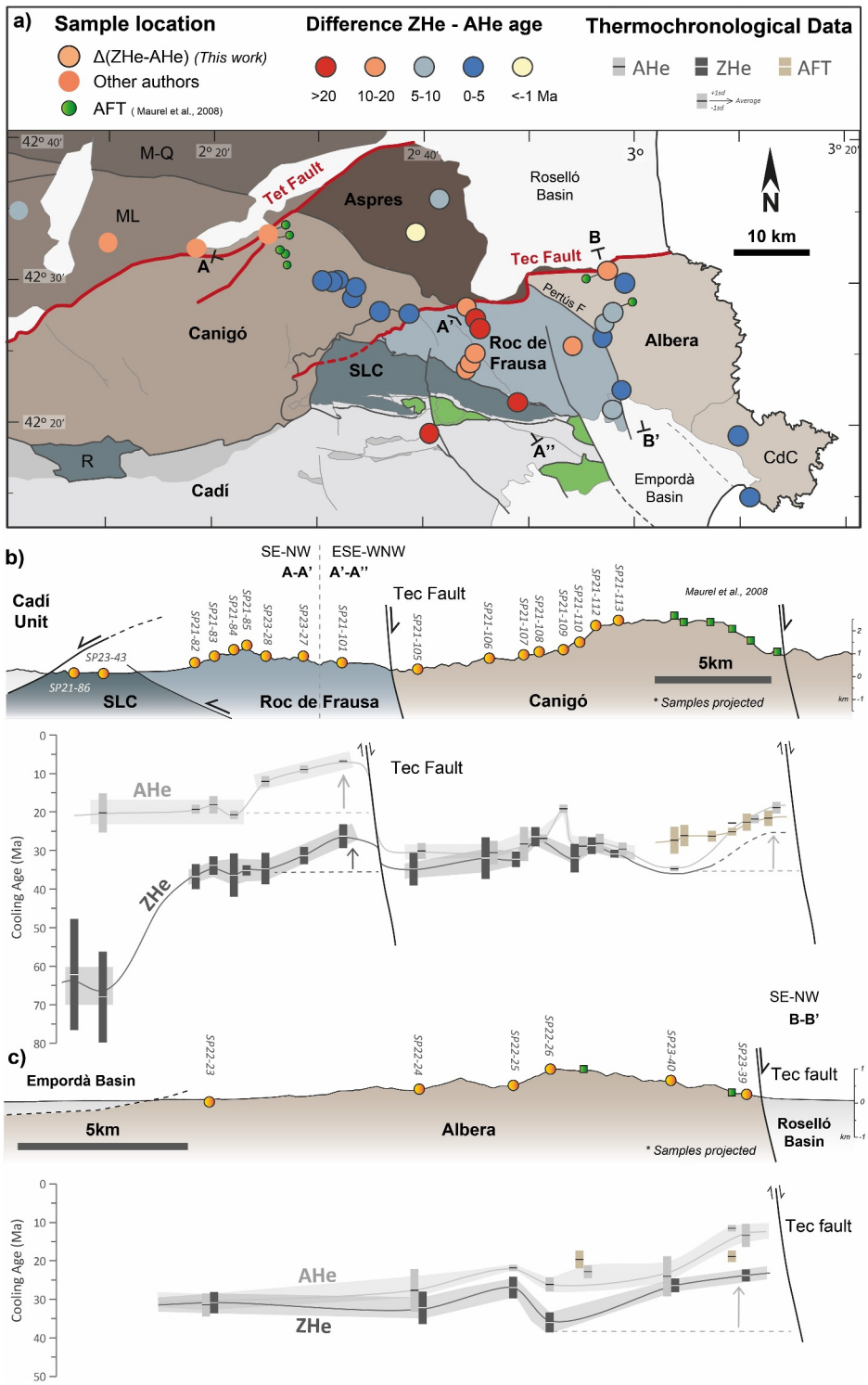

Figure 8. (a) Structural map showing the main tectonic units and the difference between the ZHe and the AHe ages, Δ(ZHe-AHe), for individual samples. See Figure 4 or Figure 6 for a color legend of tectonic units. (b) Topographic profile with projected (U-Th)/He ages from the Canigó to the Sant Llorenç de Cerdans unit (indicated in the map by A-A′-A′′). (c) Profile for the Albera unit (B-B′). Vertical arrows in the footwall indicate the younger ages toward the fault. See the main text for further explanation.

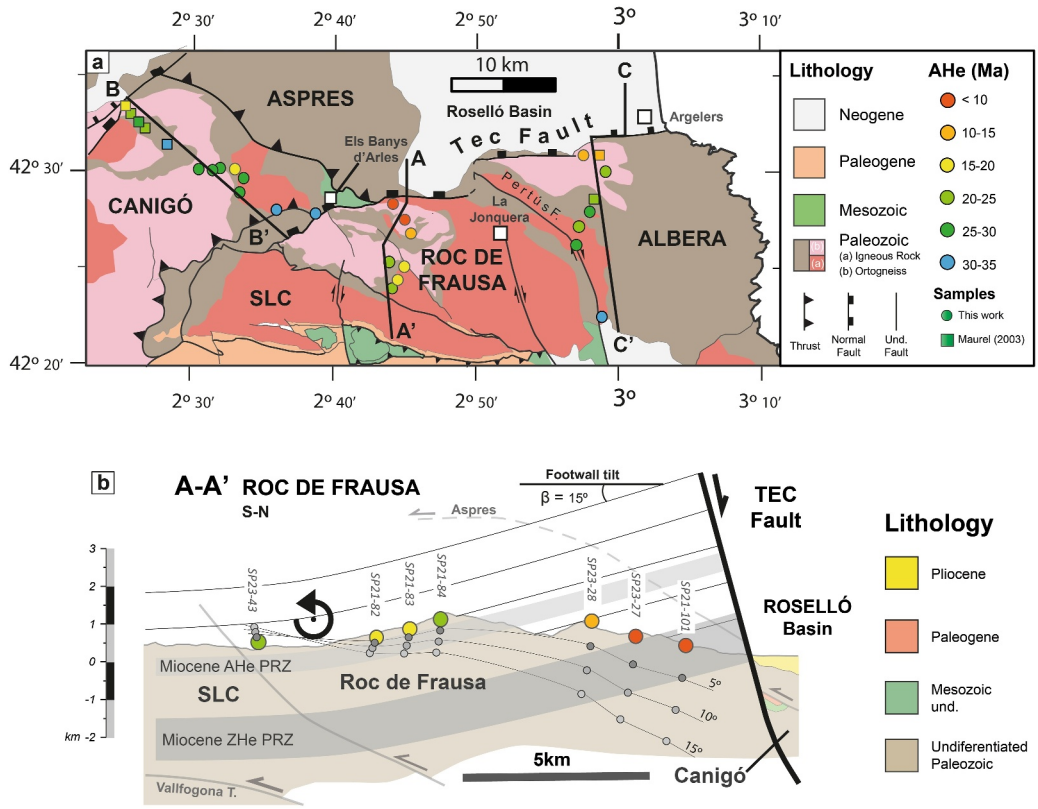

Figure 9. (a) Geologic map of the Eastern Pyrenees (Canigó, Roc de Frausa and Albera massifs), enlarged from Figure 2. AHe samples location from this study (circles) and Maurel (2003) (squares) are shown. (b) Roc de Frausa profile A-A′, showing in gray the interpreted "fossil" AHe and ZHe partial retention zone. The gray circles represent a visual representation of footwall block rotation, showing the interpreted structural depth for each sample for different degrees of tilting (5°, 10°, 15°). The position of the axis of rotation position is speculated, and its distance respect to the fault plane is interpreted to be 12 km. Profiles B-B′ and C-C′ are presented in Supporting Information S1 (Figures S4). See the main text for discussion.

fault plane, without evidence of hydrothermal alteration, and both ZHe and AHe show similar trends, they can be interpreted to record the fault footwall uplift and consequent thermal evolution.

5.3. Significance of Block Rotation During Normal Faulting

As mentioned above, an additional factor to consider when estimating apparent exhumation rates in normal faulting is the potential tilting or rotation of footwall blocks (Johnstone & Colgan, 2018). To improve accuracy, structural depth, defined as the depth of samples relative to a relative pre-tectonic surface, was used instead of the present-day elevation of these samples in the age-elevation profiles. In general, an increase in footwall tilting and/or distance from the rotation axis results in greater structural depth (Figure 9). The slope breaks observed in the age-structural depth profiles are commonly interpreted as marking the onset of normal faulting (Stockli, 2005). Segments with low slope are typically attributed to an "older" exhumed PRZ. Apparent exhumation rates are calculated using the high-slope segments (Johnstone & Colgan, 2018). Our low-temperature thermochronological data set from the footwall of the Tec fault provides a robust basis for evaluating the effect of fault-block rotation on both AHe and ZHe cooling ages. This, in turn, allows us to refine the estimated apparent exhumation rates and better constrain the onset of normal faulting.

Figures 9 and 10 summarize the effect of block rotation on the Roc de Frausa massif, while the Canigó and Albera blocks are shown in the Figure S3 in Supporting Information S1. Structural depths of samples were calculated assuming rigid rotation of the fault footwalls, following the approach used by Johnstone & Colgan (2018). The pre-Miocene erosional surface from Calvet et al. (2021) was selected as the reference for structural depth calculation. The rotation axis was tentatively located assuming it corresponds to the slope break of the topography

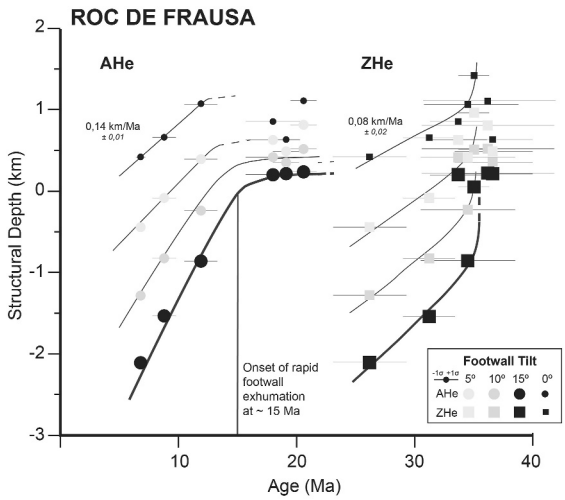

Figure 10. Age-elevation profile for the Roc de Frausa massif using the structural depth, which was obtained graphically. The calculated slope value (apparent exhumation) represents the best-fitting line. The rest of the slopes (black lines) are assumed.

at the base of the mountain massifs (Figure 9 and Figure S3 in Supporting Information S1). For the Roc de Frausa case, the distance between the fault and the rotation axis is approximately 12 km, which is consistent with the estimated maximum fault slip (ca. 1.6 km) (Lacan & Ortuño, 2012). To infer the tilt angle of the fault blocks, we used the rotation observed in the seismic reflection profile published by Calvet et al. (2022) across the Roselló Basin (Figure 9). This profile shows a series of tilted basement blocks inclined from 10° to 35° to the north. Consistently, the pre-Miocene erosional surface at Roc de Frausa shows a tilting between 10° and 15°.

We calculated three distinct structural depths for each sample, corresponding to three specific tilting angles: 5°, 10° and 15° (Figure 10). In the age-structural depth diagram (Figure 10), the observed AHe break in slope suggests the onset of rapid footwall exhumation at ca. 15 Ma. In contrast, the ZHe data exhibit a break in slope from high to low gradients, indicating that the younger samples were located within the pre-extension PRZ (Figure 9).

For cases involving large tilting (i.e., 15° of rotation), the apparent exhumation rates on the northern flank of Roc de Frausa massif are slightly higher than previously estimated using the age-elevation profile (see Figure 4). Conversely, on the southern flank, the nearly vertical or even negative slopes observed in the age-elevation profiles (Figure 4) become flatter, as samples exhibit minimal depth differences in the age-structural depth diagrams. A plausible explanation for these steep or negative slopes is to invoke a rotation of the erosional paleosurface due to fault footwall tilting. This implies that the southern flank of the Roc de Frausa massif may essentially represent an early Miocene paleosurface, consistent with the interpretation by Calvet et al. (2021) for similar surfaces elsewhere in the Eastern Pyrenees.

Additionally, we assessed the impact of tilting on thermal histories by conducting a new set of *QTQt* simulations. These simulations combined the northern and southern profiles of Roc de Frausa, using structural depths instead of actual topographic elevations. The results for a 15° rotation scenario are presented in Figure S4 in Supporting Information S1. The modeling cooling events closely resemble those previously obtained (Figure 7), confirming a rapid cooling during the Oligocene (38–32 Ma), followed by a period of slow cooling or quiescence from 32 to 22 Ma, and renewed cooling subdivided into two stages at 22–16 Ma and 12–8 Ma.

5.4. Geodynamic Implications: The Transition From Compression to Extension in the Eastern Pyrenees

The present-day structure of the Eastern Pyrenees is influenced by the superposition of the orogenic compressional phase and a subsequent post-orogenic extension. The magnitude of the orogenic shortening in the Eastern Pyrenees, and its comparison with the Central Pyrenees, remains uncertain, and this links with the problem of the absence of a crustal root in the former. While Pedrera et al. (2023) proposed an eastward shortening reduction in the Central Pyrenees (<100 km in an easternmost profile), Vergés et al. (1995) and Grool et al. (2018) estimated 111 or 125 km of shortening in a profile located further east, within the Eastern Pyrenees. On the other hand, Ternois et al. (2019) reported a crustal shortening of only 43 km even farther east. However, as the authors acknowledge, this estimate does not account for the shortening acquired by the closure of the exhumed mantle domain between the Pyrenean margins. Ford et al. (2022) also noted that crustal shortening in that area could not be confidently quantified due to limited exposure of post-basement structures. It is thus debated whether the lack of crustal root in the Eastern Pyrenees is due to limited shortening (Pedrera et al., 2023), to shortening transfer south of the Pyrenean domain (Chevrot et al., 2018), to root removal during the post-orogenic extension (L. Jolivet et al., 2020), or to the original, pre-orogenic thinned configuration (Díaz et al., 2018). Although our data do not allow us to discriminate between these hypotheses, the observed ZHe reset by nappe stacking across much of the Axial Zone, along with the high exhumation values inferred, support that a significant shortening structure is still to be considered in the Eastern Pyrenees.

Previous authors (e.g., Maurel et al., 2008; Milesi et al., 2022) have reported three principal cooling phases in the footwall of the Tet fault: Priabonian-Oligocene (~35–28 Ma), Oligo-Miocene (26–19 Ma) and finally Serravallian-Tortonian (12–9 Ma) (Figure 7). All these three cooling phases were interpreted as related to rifting and extensional movement at the Tet fault. Milesi et al. (2022) suggest that an exhumation related to southward

10.1029/2025TC009000

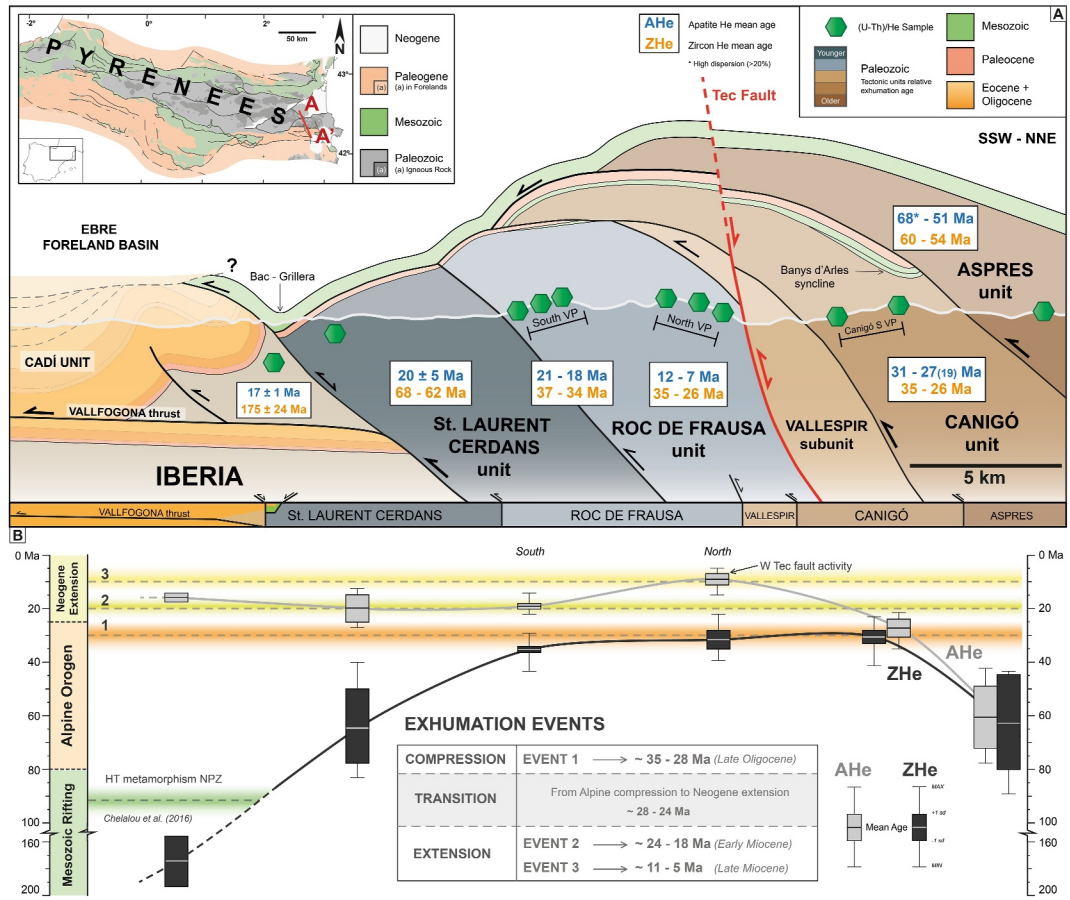

Figure 11. (a) Schematic cross-section (A-A′) showing the main tectonic units and the range of ages obtained from the study samples and profiles (section location in inset map of the Eastern Pyrenees) (b) Summary of the mean apatite and zircon (U-Th)/He ages obtained from our samples along the section, grouped in tectonic units and sample profiles. Also indicated are main exhumation events deduced in this work (boxed).

thrusting along the Tet fault ended at 35 Ma (Priabonian), due to the general onset of the West European Rift System (Ziegler, 1992). Then, since the Oligocene, the subsequent cooling events were interpreted as product of the postorogenic rifting and the opening of the Gulf of Lion (Gunnell et al., 2009; Maurel et al., 2008; Milesi et al., 2022).

Our thermochronological data and thermal models also indicate the occurrence of three main cooling events (Figure 11): (a) Priabonian-Rupelian (35–28 Ma), (b) Oligo-Miocene (24–18 Ma), and (c) late Miocene (11–5 Ma). Nevertheless, diverse aspects of our results suggest that the Paleogene cooling phase from 35 to 28 Ma was still entirely related with the Alpine shortening, instead of comprising the onset of extension. First, the spatial distribution of ZHe ages exhibit a north-to-south decreasing trend, with the exception of the SLC and Cadí units (Figure 11), which record only partial reset or no reset. As indicated above, the degree of reset is related to the degree of overlap of the different thrust units (i.e., the leading edge of the antiformal nappe stack did not reach the SLC), and the observed trends are still consistent with a piggy-back propagation of thrusting in the Iberian margin. Secondly, the Canigó and Albera units show similar ZHe and AHe ages indicating a fast exhumation event from ∼35 to 28 Ma. This cooling event affected a large region of the Eastern Pyrenees that currently is on both sides of the Tec fault, so the event cannot be simply related to the onset of Tec normal faulting. Lastly, the larger Δ(ZHe-AHe) lag time recorded in Roc de Frausa indicates that this unit remained below the apatite PRZ after the Paleogene fast cooling event, and finally exhumed during the Oligo-Miocene, similarly to the SPZ and related with the dismantling of the south Pyrenean foreland basin. Therefore, this period of relative quiescence or slower exhumation recorded in Roc de Frausa can be regarded as the transition between compression to extension in the Eastern Pyrenees.

Other indicators also support that the Eastern Pyrenees were still affected by shortening during the Rupelian. For instance, a magnetostratigraphic study conducted 60 km southwest of the study area at the Eastern Pyrenean thrust front indicated that the synorogenic conglomerates of the upper Berga Fm. are younger than 31 Ma (Carrigan et al., 2016). Illite gouge ages from the frontal thrust as young as 31.9 ± 3.9 Ma were reported by Haines & Van Der Pluijm (2023). These latter authors interpret a period of accelerated fault displacement around 35 Ma, which is coincident with the onset of the late Eocene cooling event that we observe. Moreover, the Pertús shear zone (Figure 3), between the Roc de Frausa and Albera units, a youngest biotite Ar-Ar age was determined at 38.6 ± 0.5 Ma (Maurel, 2003). This Ar-Ar age indicates that the dextral transpressive motion reported along the fault was active synchronously with the first cooling event recorded in Roc de Frausa (40–34 Ma), supporting that the initial cooling phase recorded in Roc de Frausa is related to compression. On the other hand, this period of cooling between Priabonian and Rupelian times is recorded all along the Pyrenean orogen as the maximum exhumation peak, from the Western (Bosch et al., 2016; Guàrdia, 2024), to the Central Pyrenees (Cochelin et al., 2018; Fitzgerald et al., 1999; Gibson et al., 2007; Morris et al., 1998; Sinclair, 2005). Therefore, the conjunction of our results and these arguments support that at least until the Rupelian (∼28 Ma), exhumation in the Eastern Pyrenees was caused by crustal thickening in a compressive tectonic regime.

We conclude that a transition interval from orogenic shortening to extension-related exhumation occurred in Chattian times (∼28–24 Ma) (Figure 11), marked by an abrupt deceleration of the cooling rates. This transitional phase is recorded in the thermal evolution of the entire Eastern Pyrenees, including the Canigó, Albera, and Roc de Frausa units (Figure 7). Evidence of cooling rates deceleration from Rupelian to Chattian has also been documented in the Central Pyrenees (Aneto-Maladeta massif) (Fitzgerald et al., 1999; Gibson et al., 2007), thus indicating a regional extent along the Pyrenean chain. In the West-Central Pyrenees, this period of slow cooling is not related to the end of compression, but rather the shortening is still active until the lower Miocene (Labaume et al., 2016). Therefore, the observed deceleration in the cooling rates in the Eastern Pyrenees does not exclude the possibility that compression was still active when the transition stage here defined started.

Moreover, this transition period coincides with the timing of the formation of the range-top low-relief erosional surface "S" in the Pyrenees, as defined by Calvet et al. (2021). Assuming stable base levels during this time, it can be inferred that weathering and fluvial denudation were intense and rapid yet not counteracted by crustal uplift. This would result in low-relief topography. Although these low-relief surfaces are better preserved north of the Tet Fault than in the study area to the south (Calvet et al., 2021), the period of tectonic quiescence or slow cooling is still detected in low-T thermochronology. This has important geomorphological implications, reinforcing the hypothesis of an early Neogene uplift of low-relief surfaces proposed by these authors for the Eastern Pyrenees.

At variance from the Central Pyrenees, following this quiescence period, a re-acceleration of the cooling rates is recorded at ∼24 Ma (latest Chattian) in the Eastern Pyrenees, marking the onset of a new phase of exhumation that we unequivocally link to the extension. The first evidence indicating that this phase is associated with extension is the decrease of AHe and ZHe ages toward the Tec and Tet fault footwalls, which is characteristic of extensional systems (e.g., Ehlers et al., 2001; Stockli, 2005). The second evidence is the similar AHe age (∼20–18 Ma) observed in Roc de Frausa, SLC, and Cadí units, which are separated by major thrust faults indicating that cooling is unrelated to shortening and also affected the foreland basin. The third evidence is the trend of AHe ages observed in the Tec fault, evolving from 13 Ma in the eastern segment (Albera), to 6 Ma in the western segment (Roc de Frausa). A westward evolution of extension is expected for the rifting propagating from the Gulf of Lion, although this trend is not evident in a regional frame beyond the Tec fault footwall. The fourth piece of evidence relates with the spatial distribution of the lag time Δ(ZHe-AHe): while the Albera and Canigó units show a small lag time that indicates a rapid cooling, the samples located in the southern units display a large lag time, which evidences that they remained at depths below the apatite PRZ until this second cooling phase. Lastly, the lag time Δ(ZHe-AHe) increases near the footwall of the Tec fault, which suggests the presence of an exhumed apatite PRZ since AHe ages decreases rapidly with little vertical offset (Fitzgerald & Malusà, 2019). This phenomenon is occasionally observed in the footwall of normal faults (Stockli, 2005), and potentially can be used to estimate footwall tilting.

The relationship between this new phase of cooling and the extension is supported by the intramontane tectono-stratigraphic evolution of the Eastern Pyrenean domain (Calvet et al., 2021). The cooling event from the Chattian to early Miocene is contemporaneous with the first dated sediments in the adjacent Roselló and Conflent basins (Aquitanian). Finally, the youngest cooling event in Tortonian–Messinian times is coeval with the opening

of the Cerdanya and la Seu basins (Calvet et al., 2021), and the opening of the Empordà basin in the SPZ (Fleta et al., 1991; Saula et al., 1994) (Figure 1). It is worth underlining that the apparent exhumation rates calculated for this event for the Albera and Roc de Frausa footwalls (~0.1 km/Ma), are similar to those calculated for the Tet footwall in the Canigó unit (0.1–0.3 km/Ma) by Milesi et al. (2022).

6. Conclusions

Based on new ZHe and AHe data combined with inverse thermal modeling, we refine the differentiation of basement-involved thrust sheets in the Axial Zone of the Eastern Pyrenees and discuss the timing for the transition from compressional mountain building to the post-orogenic extension in relation to the Gulf of Lyon rifting. Our results reveal at least three main cooling events with distinct exhumation paths across the tectonic units. We propose that a principal cooling/exhumation event between Priabonian and Rupelian is still related to the Pyrenean Alpine shortening, affecting the entire southern Axial Zone, from the Roc de Frausa (39–34 Ma) to the Albera and Canigó units (34–28 Ma). A marked slowdown in cooling during Chattian times (28–24 Ma) precedes a second cooling phase, which we associate with the onset of the post-orogenic extension. This second phase of cooling (24–18 Ma) is observed in the southern units of the Axial Zone located in the footwall of the Tec normal fault, as well as in the SPZ (Cadí unit). These findings suggest a transition period of ca. 4 Ma characterized by quiescence or slow cooling during the shift from compressional to extensional tectonic regimes in the Eastern Pyrenees, while compression persisted in the Central Pyrenees. A late cooling event between 11 and 5 Ma is recorded exclusively in the immediate footwall of the Tec normal fault at Roc de Frausa and Albera massifs during the late Miocene (Tortonian-Messinian), providing evidence for the Tec fault reactivation and southwestward propagation.

Conflict of Interest

The authors declare no conflicts of interest relevant to this study.

Data Availability Statement

The reduced apatite and zircon (U-Th)/He data from the Eastern Pyrenees is available in Peris (2025) on the Mendeley Database (https://doi.org/10.17632/7mdyx8xt43.2). License: CC BY 4.0.

Acknowledgments
This work was financed by the Spanish MCIU projects PGC2018-093903-B-C21 and PID2021-122467NB-C21. S. Peris benefitted from an FPU doctoral grant (FPU19/05151) from the Spanish MCIU. We thank Marc Guàrdia and Norbert Caldera for assistance in the field, and Lisa Stockli and Rudra for assistance during the (U-Th)/He analysis and for fruitful discussions. The comments by the reviewers Frederic Mouthereau, Yanni Gunnell, and Antonio Pedrera, as well as by the editor Federico Rossetti and the associate editor Eva Enkelmann helped to improve this manuscript.

References

Abbey, A. L., Wildman, M., Stevens Goddard, A. L., & Murray, K. E. (2023). Thermal history modeling techniques and interpretation strategies: Applications using QTQt. *Geosphere*, *19*(2), 493–530. https://doi.org/10.1130/GES02528.1

Angrand, P., Ford, M., & Watts, A. B. (2018). Lateral variations in foreland flexure of a rifted Continental margin: The Aquitaine basin (SW France). *Tectonics*, *37*(2), 430–449. https://doi.org/10.1002/2017TC004670

Angrand, P., & Mouthereau, F. (2021). Evolution of the alpine orogenic belts in the Western Mediterranean region as resolved by the kinematics of the Europe-Africa diffuse plate boundary. *BSGF–Earth Sciences Bulletin*, *192*, 42. https://doi.org/10.1051/bsgf/2021031

Beamud, E., Muñoz, J. A., Fitzgerald, P. G., Baldwin, S. L., Garcés, M., Cabrera, L., & Metcalf, J. R. (2011). Magnetostratigraphy and detrital apatite fission track thermochronology in syntectonic conglomerates: Constraints on the exhumation of the South-Central Pyrenees: South-central Pyrenees magnetostratigraphy and thermochronology. *Basin Research*, *23*(3), 309–331. https://doi.org/10.1111/j.1365-2117.2010.00492.x

Beaumont, C., Muñoz, J. A., Hamilton, J., & Fullsack, P. (2000). Factors controlling the alpine evolution of the central pyrenees inferred from a comparison of observations and geodynamical models. *Journal of Geophysical Research*, *105*(B4), 8121–8145. https://doi.org/10.1029/1999JB900390

Birot, P. (1937). *Recherches sur la morphologie des Pyrénées orientales franco-espagnoles [Doctorat Ès Lettres Thesis]*. Faculté des Lettres de l'Université de Paris.

Bolós, X., Martí, J., Becerril, L., Planagumà, L., Grosse, P., & Barde-Cabusson, S. (2015). Volcano-structural analysis of La Garrotxa Volcanic Field (NE Iberia): Implications for the plumbing system. *Tectonophysics*, *642*, 58–70. https://doi.org/10.1016/j.tecto.2014.12.013

Bosch, G., Teixell, A., Jolivet, M., Labaume, P., Stockli, D., Domènech, M., & Monié, P. (2016). Timing of Eocene–Miocene thrust activity in the Western axial zone and Chaînons Béarnais (West-central Pyrenees) revealed by multi-method thermochronology. *Comptes Rendus Geoscience*, *348*(3–4), 246–256. https://doi.org/10.1016/j.crte.2016.01.001

Calvet, M. (1996). Morphogenèse d'une montagne méditerranéenne: Les Pyrénées orientales [Thèse doctorat état 1994]. *Documents du BRGM n° 225, Órleans*.

Calvet, M., Delmas, M., Gunnell, Y., & Laumonier, B. (2022). *Geology and landscapes of the Eastern pyrenees: A field guide with excursions*. Springer International Publishing. https://doi.org/10.1007/978-3-030-84266-6

Calvet, M., Gunnell, Y., & Laumonier, B. (2021). Denudation history and palaeogeography of the Pyrenees and their peripheral basins: An 84-million-year geomorphological perspective. *Earth-Science Reviews*, *215*, 103436. https://doi.org/10.1016/j.earscirev.2020.103436

Carrigan, J. H., Anastasio, D. J., Kodama, K. P., & Parés, J. M. (2016). Fault-related fold kinematics recorded by terrestrial growth strata, Sant Llorenç de Morunys, Pyrenees Mountains, NE Spain. *Journal of Structural Geology*, *91*, 161–176. https://doi.org/10.1016/j.jsg.2016.09.003

Chelalou, R., Nalpas, T., Bousquet, R., Prevost, M., Lahfid, A., Poujol, M., et al. (2016). New sedimentological, structural and paleo-thermicity data in the Boucheville basin (eastern North Pyrenean zone, France). *Comptes Rendus Geoscience*, *348*(3–4), 312–321. https://doi.org/10.1016/j.crte.2015.11.008

Chevrot, S., Sylvander, M., Diaz, J., Martin, R., Mouthereau, F., Manatschal, G., et al. (2018). The non-cylindrical crustal architecture of the Pyrenees. *Scientific Reports*, *8*(1), 9591. https://doi.org/10.1038/s41598-018-27889-x

Choukroune, P. (1989). The Ecors Pyrenean deep seismic profile reflection data and the overall structure of an orogenic belt. *Tectonics*, *8*(1), 23–39. https://doi.org/10.1029/TC008i001p00023

Clerc, C., Lahfid, A., Monié, P., Lagabrielle, Y., Chopin, C., Poujol, M., et al. (2015). High-temperature metamorphism during extreme thinning of the continental crust: A reappraisal of the North Pyrenean passive paleomargin. *Solid Earth*, *6*(2), 643–668. https://doi.org/10.5194/se-6-643-2015

Cochelin, B., Lemirre, B., Denèle, Y., De Saint Blanquat, M., Lahfid, A., & Duchêne, S. (2018). Structural inheritance in the Central Pyrenees: The Variscan to alpine tectonometamorphic evolution of the axial zone. *Journal of the Geological Society*, *175*(2), 336–351. https://doi.org/10.1144/jgs2017-066

Cruset, D., Vergés, J., Albert, R., Gerdes, A., Benedicto, A., Cantarero, I., & Travé, A. (2020). Quantifying deformation processes in the SE Pyrenees using U–Pb dating of fracture-filling calcites. *Journal of the Geological Society*, *177*(6), 1186–1196. https://doi.org/10.1144/jgs2020-014

Curry, M. E., Beek, P. V. D., Huismans, R. S., Wolf, S. G., Fillon, C., & Muñoz, J.-A. (2021). Spatio-temporal patterns of Pyrenean exhumation revealed by inverse thermo-kinematic modeling of a large thermochronologic data set. *Geology*, *49*(6), 738–742. https://doi.org/10.1130/G48687.1

Dewey, J. F. (1988). Extensional collapse of orogens. *Tectonics*, *7*(6), 1123–1139. https://doi.org/10.1029/TC007i006p01123

Diaz, J., Vergés, J., Chevrot, S., Antonio-Vigil, A., Ruiz, M., Sylvander, M., & Gallart, J. (2018). Mapping the crustal structure beneath the eastern Pyrenees. *Tectonophysics*, *744*, 296–309. https://doi.org/10.1016/j.tecto.2018.07.011

Dodson, M. H. (1973). Closure temperature in cooling geochronological and petrological systems. *Contributions to Mineralogy and Petrology*, *40*(3), 259–274. https://doi.org/10.1007/BF00373790

Ehlers, T. A., Armstrong, P. A., & Chapman, D. S. (2001). Normal fault thermal regimes and the interpretation of low-temperature thermochronometers. *Physics of the Earth and Planetary Interiors*, *126*(3–4), 179–194. https://doi.org/10.1016/S0031-9201(01)00254-0

Farley, K. A. (2000). Helium diffusion from apatite: General behavior as illustrated by Durango fluorapatite. *Journal of Geophysical Research*, *105*(B2), 2903–2914. https://doi.org/10.1029/1999JB900348

Farley, K. A., Wolf, R. A., & Silver, L. T. (1996). The effects of long alpha-stopping distances on (U-Th)/He ages. *Geochimica et Cosmochimica Acta*, *60*(21), 4223–4229. https://doi.org/10.1016/S0016-7037(96)00193-7

Filleaudeau, P., Mouthereau, F., & Pik, R. (2012). Thermo-tectonic evolution of the south-central Pyrenees from rifting to orogeny: Insights from detrital zircon U/Pb and (U-Th)/He thermochronometry. *Basin Research*, *24*(4), 401–417. https://doi.org/10.1111/j.1365-2117.2011.00535.x

Fillon, C., Mouthereau, F., Calassou, S., Pik, R., Bellahsen, N., Gautheron, C., et al. (2021). Post-orogenic exhumation in the western Pyrenees: Evidence for extension driven by pre-orogenic inheritance. *Journal of the Geological Society*, *178*(2), 2020–2079. https://doi.org/10.1144/jgs2020-079

Fitzgerald, P. G., & Malusà, M. G. (2019). Concept of the exhumed partial annealing (Retention) zone and age-elevation profiles in thermochronology. In M. G. Malusà & P. G. Fitzgerald (Eds.), *Fission-track thermochronology and its application to geology* (pp. 165–189). Springer International Publishing. https://doi.org/10.1007/978-3-319-89421-8_9

Fitzgerald, P. G., Muñoz, J. A., Coney, P. J., & Baldwin, S. L. (1999). Asymmetric exhumation across the Pyrenean orogen: Implications for the tectonic evolution of a collisional orogen. *Earth and Planetary Science Letters*, *173*(3), 157–170. https://doi.org/10.1016/S0012-821X(99)00225-3

Fleta, J., Arasa Tuliesa, A., & Escuer, J. (1991). El Neógeno del Empordà y Baix Ebre (Catalunya): Estudio comparativo. *Acta Geologica Hispanica*, *26*(3–4), 159–171.

Flowers, R. M., Ketcham, R. A., Enkelmann, E., Gautheron, C., Reiners, P. W., Metcalf, J. R., et al. (2023). (U-Th)/He chronology: Part 2. Considerations for evaluating, integrating, and interpreting conventional individual aliquot data. *GSA Bulletin*, *135*(1–2), 137–161. https://doi.org/10.1130/B36268.1

Flowers, R. M., Zeitler, P. K., Danišík, M., Reiners, P. W., Gautheron, C., Ketcham, R. A., et al. (2023). (U-Th)/He chronology: Part 1. Data, uncertainty, and reporting. *GSA Bulletin*, *135*(1–2), 104–136. https://doi.org/10.1130/B36266.1

Ford, M., Hemmer, L., Vacherat, A., Gallagher, K., & Christophoul, F. (2016). Retro-wedge foreland basin evolution along the ECORS line, eastern Pyrenees, France. *Journal of the Geological Society*, *173*(3), 419–437. https://doi.org/10.1144/jgs2015-129

Ford, M., Masini, E., Vergés, J., Pik, R., Ternois, S., Léger, J., et al. (2022). Evolution of a low convergence collisional orogen: A review of Pyrenean orogenesis. *BSGF–Earth Sciences Bulletin*, *193*, 19. https://doi.org/10.1051/bsgf/2022018

Gallagher, K. (2012). Transdimensional inverse thermal history modeling for quantitative thermochronology. *Journal of Geophysical Research*, *117*(B2), 2011JB008825. https://doi.org/10.1029/2011JB008825

Gallagher, K., Charvin, K., Nielsen, S., Sambridge, M., & Stephenson, J. (2009). Markov chain Monte Carlo (MCMC) sampling methods to determine optimal models, model resolution and model choice for Earth Science problems. *Marine and Petroleum Geology*, *26*(4), 525–535. https://doi.org/10.1016/j.marpetgeo.2009.01.003

Gibson, M., Sinclair, H. D., Lynn, G. J., & Stuart, F. M. (2007). Late- to post-orogenic exhumation of the Central Pyrenees revealed through combined thermochronological data and modelling. *Basin Research*, *19*(3), 323–334. https://doi.org/10.1111/j.1365-2117.2007.00333.x

Grool, A. R., Ford, M., Vergés, J., Huismans, R. S., Christophoul, F., & Dielforder, A. (2018). Insights into the crustal-scale dynamics of a doubly vergent orogen from a quantitative analysis of its forelands: A case study of the Eastern pyrenees. *Tectonics*, *37*(2), 450–476. https://doi.org/10.1002/2017TC004731

Guàrdia, M. (2024). *Time constraints and dynamics of the Eaux-Chaudes nappe (West-Central Pyrenees): A study combining new tectonothermal data and thermo-mechanic simulations*. Universitat Autònoma de Barcelona.

Guenthner, W. R., Reiners, P. W., Ketcham, R. A., Nasdala, L., & Giester, G. (2013). Helium diffusion in natural zircon: Radiation damage, anisotropy, and the interpretation of zircon (U-Th)/He thermochronology. *American Journal of Science*, *313*(3), 145–198. https://doi.org/10.2475/03.2013.01

Guitard, G., Geyssant, J., Laumonier, B., Autran, A., Fonteilles, M., DalmayraC, B., et al. (1992). *Carte géol. France (1/50 000), feuille Prades (1095)*. Orléans: BRGM. Notice explicative par G. Guitard et al. (1998).

Gunnell, Y., Calvet, M., Brichau, S., Carter, A., Aguilar, J.-P., & Zeyen, H. (2009). Low long-term erosion rates in high-energy mountain belts: Insights from thermo- and biochronology in the Eastern Pyrenees. *Earth and Planetary Science Letters*, *278*(3–4), 208–218. https://doi.org/10.1016/j.epsl.2008.12.004

Gunnell, Y., Zeyen, H., & Calvet, M. (2008). Geophysical evidence of a missing lithospheric root beneath the Eastern Pyrenees: Consequences for post-orogenic uplift and associated geomorphic signatures. *Earth and Planetary Science Letters*, *276*(3–4), 302–313. https://doi.org/10.1016/j.epsl.2008.09.031

Haines, S. H., & Van Der Pluijm, B. A. (2023). Fault gouge dating in the Spanish pyrenees: Fault ages, thrust propagation sequence, Wall-Rock provenance, and thermal constraints. *Tectonics*, *42*(2), e2022TC007251. https://doi.org/10.1029/2022TC007251

Hart, N. R., Stockli, D. F., Lavier, L. L., & Hayman, N. W. (2017). Thermal evolution of a hyperextended rift basin, Mauléon Basin, western Pyrenees. *Tectonics*, *36*(6), 1103–1128. https://doi.org/10.1002/2016TC004365

ICGC. (2021). Mapa Geològic de Catalunya [Map]. Institut Cartogràfic i Geològic de Catalunya (ICGC).

ICGC. (2024). Mapa de les Unitats Estructurals majors de Catalunya [Map]. Institut Cartogràfic i Geològic de Catalunya (ICGC).

Jammes, S., Manatschal, G., Lavier, L., & Masini, E. (2009). Tectonosedimentary evolution related to extreme crustal thinning ahead of a propagating ocean: Example of the western Pyrenees. *Tectonics*, *28*(4), 2008TC002406. https://doi.org/10.1029/2008TC002406

Johnstone, S. A., & Colgan, J. P. (2018). Interpretation of low-temperature thermochronometer ages from tilted normal fault blocks. *Tectonics*, *37*(10), 3647–3667. https://doi.org/10.1029/2018TC005207

Jolivet, L., & Faccenna, C. (2000). Mediterranean extension and the Africa-Eurasia collision. *Tectonics*, *19*(6), 1095–1106. https://doi.org/10.1029/2000TC900018

Jolivet, L., Romagny, A., Gorini, C., Maillard, A., Thinon, I., Couëffé, R., et al. (2020). Fast dismantling of a mountain belt by mantle flow: Late-orogenic evolution of Pyrenees and Liguro-Provençal rifting. *Tectonophysics*, *776*, 228312. https://doi.org/10.1016/j.tecto.2019.228312

Jolivet, M., Labaume, P., Monié, P., Brunel, M., Arnaud, N., & Campani, M. (2007). Thermochronology constraints for the propagation sequence of the south pyrenean basement thrust system (France-Spain). *Tectonics*, *26*(5), 2006TC002080. https://doi.org/10.1029/2006TC002080

Juez-Larré, J., & Andriessen, P. (2006). Tectonothermal evolution of the northeastern margin of Iberia since the break-up of Pangea to present, revealed by low-temperature fission-track and (U–Th)/He thermochronologyA case history of the Catalan Coastal Ranges. *Earth and Planetary Science Letters*, *243*(1–2), 159–180. https://doi.org/10.1016/j.epsl.2005.12.026

Labaume, P., Meresse, F., Jolivet, M., Teixell, A., & Lahfid, A. (2016). Tectonothermal history of an exhumed thrust-sheet-top basin: An example from the south Pyrenean thrust belt. *Tectonics*, *35*(5), 1280–1313. https://doi.org/10.1002/2016TC004192

Lacan, P., & Ortuño, M. (2012). Active tectonics of the Pyrenees: A review. *Journal of Iberian Geology*, *38*(1), 9–30. https://doi.org/10.5209/rev_JIGE.2012.v38.n1.39203

Lagabrielle, Y., Labaume, P., & De Saint Blanquat, M. (2010). Mantle exhumation, crustal denudation, and gravity tectonics during Cretaceous rifting in the Pyrenean realm (SW Europe): Insights from the geological setting of the lherzolite bodies: Pyerenean lherzolites, gravity tectonics. *Tectonics*, *29*(4). https://doi.org/10.1029/2009TC002588

Laumonier, B. (2015). Les Pyrénées alpines sud-orientales (France, Espagne)–essai de synthèse. *Revue de Géologie pyrénéenne*, *2*(1), 44.

Laumonier, B., Baudin, T., Barbey, P., Calvet, M., & Lenoble, J. L. (2023). Notice explicative carte géol. France (1:50,000) feuille Arles-sur-Tech (n°1100), Orléans, BRGM, 194 p., Carte géologique par Baudin et al. (2009).

Laumonier, B., Calvet, M., Le Bayon, B., Barbey, P., & Lenoble, J.-L. (2015). Notice explicative, Carte géol. France (1/50 000), feuille Prats-de-Mollo-la-Preste (1099). Orléans: BRGM, 189 p. Carte géologique par Laumonier et al. (2015).

Laumonier, B., Le Bayon, B., & Calvet, M. (2015). *Carte géol. France (1/50 000), feuille prats-de-mollo-la-preste (1099)*. Orléans: BRGM. Notice explicative par Laumonier et al. (2015).

Lister, G. S., Banga, G., & Feenstra, A. (1984). Metamorphic core complexes of Cordilleran type in the Cyclades, Aegean Sea, Greece. *Geology*, *12*(4), 221. https://doi.org/10.1130/0091-7613(1984)12<221:MCCOCT>2.0.CO;2

Macchiavelli, C., Vergés, J., Schettino, A., Fernàndez, M., Turco, E., Casciello, E., et al. (2017). A new Southern north Atlantic isochron map: Insights into the drift of the Iberian plate since the Late Cretaceous. *Journal of Geophysical Research: Solid Earth*, *122*(12), 9603–9626. https://doi.org/10.1002/2017JB014769

Martí, J., Mitjavila, J., Roca, E., & Aparicio, A. (1992). Cenozoic magmatism of the Valencia trough (western mediterranean): Relationship between structural evolution and volcanism. *Tectonophysics*, *203*(1–4), 145–165. https://doi.org/10.1016/0040-1951(92)90221-Q

Maurel, O. (2003). L'exhumation de la Zone Axiale des Pyrénées orientales: Une approche thermo-chronologique multi-méthodes du rôle des failles. *Doctoral Dissertation, Université Montpellier II-Sciences et Techniques du Languedoc*.

Maurel, O., Monìè, P., Pik, R., Arnaud, N., Brunel, M., & Jolivet, M. (2008). The Meso-Cenozoic thermo-tectonic evolution of the Eastern Pyrenees: An 40Ar/39Ar fission track and (U–Th)/He thermochronological study of the Canigou and Mont-Louis massifs. *International Journal of Earth Sciences*, *97*(3), 565–584. https://doi.org/10.1007/s00531-007-0179-x

Milesi, G., Monié, P., Münch, P., Soliva, R., Taillefer, A., Bruguier, O., et al. (2020). Tracking geothermal anomalies along a crustal fault using (U − Th)/He apatite thermochronology and rare-earth element (REE) analyses: The example of the Têt fault (Pyrenees, France). *Solid Earth*, *11*(5), 1747–1771. https://doi.org/10.5194/se-11-1747-2020

Milesi, G., Monié, P., Soliva, R., Münch, P., Valla, P. G., Brichau, S., et al. (2022). Deciphering the Cenozoic exhumation history of the Eastern pyrenees along a crustal-scale normal fault using low-temperature thermochronology. *Tectonics*, *41*(4), e2021TC007172. https://doi.org/10.1029/2021TC007172

Milesi, G., Münch, P., Charpentier, D., Iemmolo, A., Bouaoudi, A., Lecomte, A., et al. (2025). A long history of ductile and brittle deformation of Eastern Pyrenees fault zones: Coupling 40Ar/39Ar geochronology, chlorite geothermometry and structural observation. *Journal of Structural Geology*, *199*, 105465. https://doi.org/10.1016/j.jsg.2025.105465

Milesi, G., Valla, P. G., Münch, P., & Huyghe, D. (2023). Tectono-geomorphological evolution of the Eastern Pyrenees: Insights from thermo-kinematic modeling. *Tectonophysics*, *866*, 230057. https://doi.org/10.1016/j.tecto.2023.230057

Miranda-Muruzábal, M., Geyer, A., Aulinas, M., Albert, H., Vilà, M., Micheo, F., et al. (2024). CatVolc: A new database of geochemical and geochronological data of volcanic-related materials from the Catalan Volcanic zone (Spain). *Journal of Volcanology and Geothermal Research*, *446*, 107998. https://doi.org/10.1016/j.jvolgeores.2023.107998

Monié, P., Münch, P., Milesi, G., Bonno, M., & Iemmolo, A. (2024). 40 Ar/39 Ar geochronology of crustal deformation. *Comptes Rendus Geoscience*, *356*(S2), 495–524. https://doi.org/10.5802/crgeos.209

Morris, R. G., Sinclair, H. D., & Yelland, A. J. (1998). Exhumation of the Pyrenean orogen: Implications for sediment discharge. *Basin Research*, *10*(1), 69–85. https://doi.org/10.1046/j.1365-2117.1998.00053.x

Mouthereau, F., Filleaudeau, P.-Y., Vacherat, A., Pik, R., Lacombe, O., Fellin, M. G., et al. (2014). Placing limits to shortening evolution in the Pyrenees: Role of margin architecture and implications for the Iberia/Europe convergence: Plate convergence in the Pyrenees. *Tectonics*, *33*(12), 2283–2314. https://doi.org/10.1002/2014TC003663

Muñoz, J. A. (1992). Evolution of a continental collision belt: ECORS-Pyrenees crustal balanced cross-section. In K. R. McClay (Ed.), *Thrust tectonics* (pp. 235–246). Springer. https://doi.org/10.1007/978-94-011-3066-0_21

Muñoz, J. A., Martinez, A., & Verges, J. (1986). Thrust sequences in the eastern Spanish Pyrenees. *Journal of Structural Geology*, *8*(3–4), 399–405. https://doi.org/10.1016/0191-8141(86)90058-1

Parizot, O., Missenard, Y., Haurine, F., Blaise, T., Barbarand, J., Benedicto, A., & Sarda, P. (2021). When did the Pyrenean shortening end? Insight from U–Pb geochronology of syn-faulting calcite (Corbières area, France). *Terra Nova*, *33*(6), 551–559. https://doi.org/10.1111/ter.12547

Pedrera, A., García-Senz, J., Pueyo, E. L., López-Mir, B., Silva-Casal, R., & Díaz-Alvarado, J. (2023). Inhomogeneous rift inversion and the evolution of the Pyrenees. *Earth-Science Reviews*, *245*, 104555. https://doi.org/10.1016/j.earscirev.2023.104555

Peris, S. (2025). Low-temperature thermochronological data from the Eastern Pyrenees: Apatite and zircon (U-Th)/He [Dataset]. *Mendeley Data*. https://doi.org/10.17632/7mdyx8xt43.2

Prior, M. G., Stockli, D. F., & Singleton, J. S. (2016). Miocene slip history of the Eagle Eye detachment fault, Harquahala Mountains metamorphic core complex, west-central Arizona. *Tectonics*, *35*(8), 1913–1934. https://doi.org/10.1002/2016TC004241

Puigdefàbregas, C., Muñoz, J. A., & Vergés, J. (1992). Thrusting and foreland basin evolution in the Southern Pyrenees. In K. R. McClay (Ed.), *Thrust tectonics* (pp. 247–254). Springer. https://doi.org/10.1007/978-94-011-3066-0_22

Réhault, J.-P., Honthaas, C., Guennoc, P., Bellon, H., Ruffet, G., Cotten, J., et al. (2012). Offshore Oligo-Miocene volcanic fields within the Corsica-Liguria Basin: Magmatic diversity and slab evolution in the western Mediterranean Sea. *Journal of Geodynamics*, *58*, 73–95. https://doi.org/10.1016/j.jog.2012.02.003

Reiners, P. W. (2005). Zircon (U-Th)/He thermochronometry. *Reviews in Mineralogy and Geochemistry*, *58*(1), 151–179. https://doi.org/10.2138/rmg.2005.58.6

Reiners, P. W., & Brandon, M. T. (2006). Using thermochronology to understand orogenic erosion. *Annual Review of Earth and Planetary Sciences*, *34*(1), 419–466. https://doi.org/10.1146/annurev.earth.34.031405.125202

Reiners, P. W., Spell, T. L., Nicolescu, S., & Zanetti, K. A. (2004). Zircon (U-Th)/He thermochronometry: He diffusion and comparisons with 40Ar/39Ar dating. *Geochimica et Cosmochimica Acta*, *68*(8), 1857–1887. https://doi.org/10.1016/j.gca.2003.10.021

Roca, E. (2001). The Northwest Mediterranean Basin (valencia trough, Gulf of Lions, and Liguro-Provençal basins): Structure and geodynamic evolution. In P. A. Ziegler, W. Cavazza, A. H. F. Robertson, & S. Crasquin-Soleau (Eds.), *Peri-tethys memoir 6: Peri-tethyan Rift/Wrench basins and passive margins, Mem* (Vol. 186, pp. 617–706).

Romagny, A., Jolivet, L., Menant, A., Bessière, E., Maillard, A., Canva, A., et al. (2020). Detailed tectonic reconstructions of the Western Mediterranean region for the last 35 Ma, insights on driving mechanisms. *BSGF–Earth Sciences Bulletin*, *191*, 37. https://doi.org/10.1051/bsgf/2020040

Roure, F., Choukroune, P., Berastegui, X., Munoz, J. A., Villien, A., Matheron, P., et al. (1989). Ecors deep seismic data and balanced cross sections: Geometric constraints on the evolution of the Pyrenees. *Tectonics*, *8*(1), 41–50. https://doi.org/10.1029/TC008i001p00041

Rushlow, C. R., Barnes, J. B., Ehlers, T. A., & Vergés, J. (2013). Exhumation of the southern Pyrenean fold-thrust belt (Spain) from orogenic growth to decay. *Tectonics*, *32*(4), 843–860. https://doi.org/10.1002/tect.20030

Saula, E., Picart, J., Mató, E., Llenas, M., Losantos, M., Berastegui, X., & Agustí, J. (1994). Evolución geodinámica de la fosa del Empordà y las Sierras Transversales. *Acta Geologica Hispanica*, *29*(2–4), 55–75.

Schildgen, T. F., Van Der Beek, P. A., Sinclair, H. D., & Thiede, R. C. (2018). Spatial correlation bias in late-cenozoic erosion histories derived from thermochronology. *Nature*, *559*(7712), 89–93. https://doi.org/10.1038/s41586-018-0260-6

Séranne, M. (1999). The Gulf of Lion continental margin (NW Mediterranean) revisited by IBS: An overview. *Geological Society, London, Special Publications*, *156*(1), 15–36. https://doi.org/10.1144/GSL.SP.1999.156.01.03

Séranne, M., Couëffé, R., Husson, E., Baral, C., & Villard, J. (2021). The transition from Pyrenean shortening to Gulf of Lion rifting in Languedoc (South France) – A tectonic-sedimentation analysis. *BSGF–Earth Sciences Bulletin*, *192*, 27. https://doi.org/10.1051/bsgf/2021017

Sinclair, H. D. (2005). Asymmetric growth of the Pyrenees revealed through measurement and modeling of orogenic fluxes. *American Journal of Science*, *305*(5), 369–406. https://doi.org/10.2475/ajs.305.5.369

Stockli, D. F. (2005). Application of low-temperature thermochronometry to extensional tectonic settings. *Reviews in Mineralogy and Geochemistry*, *58*(1), 411–448. https://doi.org/10.2138/rmg.2005.58.16

Sun, J., & Murrell, S. A. F. (1994). On the growth and collapse of wide orogenic belts. *Geophysical Journal International*, *118*(1), 255–268. https://doi.org/10.1111/j.1365-246X.1994.tb04688.x

Teixell, A. (1998). Crustal structure and orogenic material budget in the west central Pyrenees. *Tectonics*, *17*(3), 395–406. https://doi.org/10.1029/98TC00561

Teixell, A., Labaume, P., Ayarza, P., Espurt, N., De Saint Blanquat, M., & Lagabrielle, Y. (2018). Crustal structure and evolution of the Pyrenean-Cantabrian belt: A review and new interpretations from recent concepts and data. *Tectonophysics*, *724*(725), 146–170. https://doi.org/10.1016/j.tecto.2018.01.009

Teixell, A., Labaume, P., & Lagabrielle, Y. (2016). The crustal evolution of the west-central Pyrenees revisited: Inferences from a new kinematic scenario. *Comptes Rendus Geoscience*, *348*(3–4), 257–267. https://doi.org/10.1016/j.crte.2015.10.010

Ternois, S., Odlum, M., Ford, M., Pik, R., Stockli, D., Tibari, B., et al. (2019). Thermochronological evidence of early orogenesis, Eastern pyrenees, France. *Tectonics*, *38*(4), 1308–1336. https://doi.org/10.1029/2018TC005254

Vacherat, A., Mouthereau, F., Pik, R., Bernet, M., Gautheron, C., Masini, E., et al. (2014). Thermal imprint of rift-related processes in orogens as recorded in the Pyrenees. *Earth and Planetary Science Letters*, *408*, 296–306. https://doi.org/10.1016/j.epsl.2014.10.014

Vacherat, A., Mouthereau, F., Pik, R., Huyghe, D., Paquette, J.-L., Christophoul, F., et al. (2017). Rift-to-collision sediment routing in the Pyrenees: A synthesis from sedimentological, geochronological and kinematic constraints. *Earth-Science Reviews*, *172*, 43–74. https://doi.org/10.1016/j.earscirev.2017.07.004

Vergés, J., Fernàndez, M., & Martìnez, A. (2002). The Pyrenean orogen: Pre-, syn-, and post-collisional evolution. *Journal of the Virtual Explorer*, 8. https://doi.org/10.3809/jvirtex.2002.00058

Vergés, J., Millán, H., Roca, E., Muñoz, J. A., Marzo, M., Cirés, J., et al. (1995). Eastern Pyrenees and related foreland basins: Pre-syn- and post-collisional crustal-scale cross-sections. *Marine and Petroleum Geology*, *12*(8), 903–915. https://doi.org/10.1016/0264-8172(95)98854-X

Villeneuve, M., Gärtner, A., Nury, D., Fournier, F., Arlhac, P., Linnemann, U., & Caron, J. P. (2019). Age and provenance of detrital zircons from the Oligocene formations of the Marseille–Aubagne basins (SE France): Consequences on the geodynamic and palaeogeographic evolution of the northern Gondwana margin. *International Journal of Earth Sciences*, *108*(1), 187–212. https://doi.org/10.1007/s00531-018-1649-z

Vissers, R. L. M., Ganerød, M., Pennock, G. M., & Van Hinsbergen, D. J. J. (2020). Eocene seismogenic reactivation of a Jurassic ductile shear zone at Cap de Creus, Pyrenees, NE Spain. *Journal of Structural Geology*, *134*, 103994. https://doi.org/10.1016/j.jsg.2020.103994

Waldner, M., Bellahsen, N., Mouthereau, F., Bernet, M., Pik, R., Rosenberg, C. L., & Balvay, M. (2021). Central pyrenees Mountain building: Constraints from new LT thermochronological data from the axial Zone. *Tectonics*, *40*(3), e2020TC006614. https://doi.org/10.1029/2020TC006614

Wernicke, B. (1981). Low-angle normal faults in the basin and range province: Nappe tectonics in an extending orogen. *Nature*, *291*(5817), 645–648. https://doi.org/10.1038/291645a0

Whitchurch, A. L., Carter, A., Sinclair, H. D., Duller, R. A., Whittaker, A. C., & Allen, P. A. (2011). Sediment routing system evolution within a diachronously uplifting orogen: Insights from detrital zircon thermochronological analyses from the South-Central pyrenees. *American Journal of Science*, *311*(5), 442–482. https://doi.org/10.2475/05.2011.03

Wiazemsky, M., Calvet, M., Laumonier, B., Guitard, G., Autran, A., Llac, F., & Baudin, T. (2010). Carte géol. France (1/50 000), feuille Céret (1096) Orléans: BRGM. Notice explicative par Laumonier et al. (2015).

Wolf, R. A., Farley, K. A., & Kass, D. M. (1998). Modeling of the temperature sensitivity of the apatite (U–Th)/He thermochronometer. *Chemical Geology*, *148*(1–2), 105–114. https://doi.org/10.1016/S0009-2541(98)00024-2

Wolf, R. A., Farley, K. A., & Silver, L. T. (1996). Helium diffusion and low-temperature thermochronometry of apatite. *Geochimica et Cosmochimica Acta*, *60*(21), 4231–4240. https://doi.org/10.1016/S0016-7037(96)00192-5

Wolfe, M. R., & Stockli, D. F. (2010). Zircon (U–Th)/He thermochronometry in the KTB drill hole, Germany, and its implications for bulk He diffusion kinetics in zircon. *Earth and Planetary Science Letters*, *295*(1–2), 69–82. https://doi.org/10.1016/j.epsl.2010.03.025

Yelland, A. J. (1991). *Fission track thermotectonics of the iberian-eurasian plate collection*. Birkbeck-University of London.

Ziegler, P. A. (1992). European Cenozoic rift system. *Tectonophysics*, *208*(1–3), 91–111. https://doi.org/10.1016/0040-1951(92)90338-7

References From the Supporting Information

Ayala, C., Torné, M., & Roca, E. (2015). A review of the current knowledge of the crustal and lithospheric structure of the Valencia trough basin. *Boletin Geologico y Minero*, *126*(2–3), 533–552. https://doi.org/10.21701/bolgeomin.126.2-3.011

Bellahsen, N., Bayet, L., Denele, Y., Waldner, M., Airaghi, L., Rosenberg, C., et al. (2019). Shortening of the axial zone, pyrenees: Shortening sequence, upper crustal mylonites and crustal strength. *Tectonophysics*, *766*, 433–452. https://doi.org/10.1016/j.tecto.2019.06.002

Fernández, M., Marzán, I., Correia, A., & Ramalho, E. (1998). Heat flow, heat production, and lithospheric thermal regime in the Iberian Peninsula. *Tectonophysics*, *291*(1–4), 29–53. https://doi.org/10.1016/S0040-1951(98)00029-8

Fillon, C., Gautheron, C., & Van Der Beek, P. (2013). Oligocene–Miocene burial and exhumation of the Southern Pyrenean foreland quantified by low-temperature thermochronology. *Journal of the Geological Society*, *170*(1), 67–77. https://doi.org/10.1144/jgs2012-051

Mauffret, A., Durand De Grossouvre, B., Tadeu Dos Reis, A., Gorini, C., & Nercessian, A. (2001). Structural geometry in the eastern Pyrenees and western Gulf of Lion (Western Mediterranean). *Journal of Structural Geology*, *23*(11), 1701–1726. https://doi.org/10.1016/S0191-8141(01)00025-6

Flowers, R. M., Ketcham, R. A., Shuster, D. L., & Farley, K. A. (2009). Apatite (U–Th)/He thermochronometry using a radiation damage accumulation and annealing model. *Geochimica et Cosmochimica Acta*, *73*(8), 2347–2365. https://doi.org/10.1016/j.gca.2009.01.015